



## Evaluations of nonlocal electron-phonon couplings in tetracene, rubrene, and C<sub>10</sub>-DNBDT-NW based on density functional theory

Takashi Otaki <sup>1,\*</sup>, Tsubasa Terashige,<sup>2</sup> Junto Tsurumi,<sup>3</sup> Tatsuya Miyamoto,<sup>1,2</sup> Noriaki Kida,<sup>1,2</sup> Shun Watanabe,<sup>1,2</sup> Toshihiro Okamoto,<sup>1,2,4</sup> Jun Takeya,<sup>1,2,3</sup> and Hiroshi Okamoto <sup>1,2,†</sup>

<sup>1</sup>*Department of Advanced Materials Science, University of Tokyo, Kashiwa, Chiba 277-8561, Japan*

<sup>2</sup>*National Institute of Advanced Industrial Science and Technology (AIST)-University of Tokyo Advanced Operando-Measurement Technology Open Innovation Laboratory (OPERANDO-OIL), AIST, 5-1-5 Kashiwanoha, Kashiwa, Chiba 277-8561, Japan*

<sup>3</sup>*International Center of Materials Nanoarchitectonics (WPI-MANA), National Institute for Materials Science (NIMS), 1-1 Namiki, Tsukuba 305-0044, Japan*

<sup>4</sup>*PRESTO, JST, 4-1-8 Honcho, Kawaguchi, Saitama 332-0012, Japan*



(Received 8 April 2020; revised 10 November 2020; accepted 17 November 2020; published 10 December 2020)

In organic molecular semiconductors (OSCs), fluctuation of transfer integrals originating from thermally induced molecular vibrations is suggested to cause large scatterings of carriers, and to be a most important factor for the suppression of their carrier mobility. The intrinsic carrier mobility under such a fluctuation of transfer integrals is calculated using the transient localization theory, in which the estimation of transfer-integral fluctuation depending on each OSC is indispensable. In the present study, we provide a methodology to evaluate nonlocal electron-phonon couplings in OSCs using the density functional theory, which enables us to evaluate precisely the fluctuation magnitude of transfer integrals. Our method is based upon the combination of the frequency correction to reduce numerical inaccuracies in normal-mode frequencies, the extraction of tight binding parameters using maximally localized Wannier functions, and the explicit consideration of anharmonicity of phonons. We apply this method to classical OSCs, tetracene and rubrene, and a recently developed high-mobility OSC, 3,11-didecyl-dinaphtho[2,3-*d*:2',3'-*d'*]benzo[1,2-*b*:4,5-*b'*]dithiophene (C<sub>10</sub>-DNBDT-NW). We succeeded in identifying the low-frequency vibrations dominating the fluctuation of transfer integrals at room temperature, which we consider to be the main factors to limit the intrinsic mobility.

DOI: [10.1103/PhysRevB.102.245201](https://doi.org/10.1103/PhysRevB.102.245201)

### I. INTRODUCTION

Organic molecular semiconductors (OSCs) have been attracting much attention for their application to printable and flexible organic field-effect transistors (OFETs) [1]. OSCs have a relatively low carrier mobility compared to that of typical inorganic semiconductors such as silicon [2]. Therefore, high mobility OSCs are needed to expand the applications of OFETs. In recent years, it has been reported that several OSCs such as rubrene and 3,11-didecyl-dinaphtho[2,3-*d*:2',3'-*d'*]benzo[1,2-*b*:4,5-*b'*]dithiophene (C<sub>10</sub>-DNBDT-NW) have a mobility exceeding 10 cm<sup>2</sup>/V s at room temperature [3,4]. These OSCs show a Hall effect [5,6] and a negative temperature dependence of the mobility [6,7], which suggest that band transport occurs in these OSCs. However, the charge transport mechanism at room temperature in high mobility OSCs is not considered to be simple coherent band transport because the estimated values of mean free paths of carriers are comparable to or shorter than the intermolecular distances [8].

According to the transient localization theory [8–11], which has recently been proposed to explain the mechanism of charge transports in OSCs, thermally induced intermolecular

vibrations act as dynamic structural disorder, and limit the intrinsic mobility. In general, the energies of intermolecular vibrations or equivalently lattice phonons are smaller than the thermal energy at room temperature ( $kT \sim 200$  cm<sup>-1</sup>) due to weak intermolecular interactions, and, therefore, can be thermally excited. The dynamic disorder is predicted to fluctuate the transfer integral by several tens of percent [10], so it is natural to consider that it will induce a transient localization of the electronic wave function. Thus, the information of intermolecular vibrations affecting the transfer integrals and restricting the intrinsic mobility should contribute to the development of guidelines in the design of high mobility OSCs.

On the basis of these backgrounds, in the present study, we focus on the intermolecular vibrations in three typical OSCs: classical OSCs, tetracene and rubrene, and a recently developed high-mobility OSC consisting of sulfur-bridged N-shaped  $\pi$  cores and alkyl chains, C<sub>10</sub>-DNBDT-NW. C<sub>10</sub>-DNBDT-NW is a promising OSC for practical use because it meets the necessary conditions for printable and flexible OFETs: sufficient solubility for solution processes, high thermal stability, and high mobility [4,12]. In those OSCs, we theoretically identify the intermolecular vibrational modes, which strongly modulate the transfer integral by computing nonlocal electron-phonon (e-ph) couplings with density functional theory (DFT) calculations. We also calculate the infrared (IR) and Raman spectra in the low-frequency

\*otaki@okalab.k.u-tokyo.ac.jp

†okamotoh@k.u-tokyo.ac.jp

region of three kinds of OSCs. By comparing the calculated spectra with the corresponding spectra experimentally obtained, we verify the validity of the vibrational calculations.

For the reliable evaluations of e-ph coupling strengths, both the harmonic frequency and the transfer integral should be obtained with high accuracy. In OSCs, the cohesive forces of intermolecular vibrations are determined by weak van der Waals forces, so that their harmonic frequencies are small (typically less than  $100\text{ cm}^{-1}$ ), resulting in numerical errors in the harmonic-frequency calculations becoming significant. Therefore, we apply the frequency correction method [13] to low-frequency modes in order to reduce numerical inaccuracies of harmonic frequencies. Accurate transfer integrals can be calculated with maximally localized Wannier functions (MLWFs) [14–16]. In addition, we take anharmonicity into account in the calculations of transfer-integral fluctuations associated with phonons with very low frequencies ( $<10\text{ cm}^{-1}$ ).

As for the nonlocal e-ph interactions of three OSCs focused here, several studies have been reported so far in Refs. [17–19] in tetracene, Refs. [10,13,16,17,20–24] in rubrene, and Refs. [10,25] in  $C_{10}$ -DNBDT-NW. Among them, the extraction of tight binding parameters using MLWFs and the incorporation of anharmonic components of phonons were performed only in rubrene in Refs. [16,21], respectively. In  $C_{10}$ -DNBDT-NW, the normal mode calculations were done only with a force field method [25], but no DFT calculations have been reported. The comparative studies of nonlocal e-ph interactions in the three OSCs presented here, based upon the same DFT framework including the frequency correction, the MLWFs, and the anharmonicity of phonons, will give valuable information to understand different characteristics of electric conduction in various kinds of OSCs.

This paper is organized as follows. In Sec. II, we summarize the crystal structures of three OSCs. In Sec. III, we introduce calculation methods including standard normal mode analysis, the frequency correction, the computations of IR/Raman spectra, transfer integrals with MLWFs, nonlocal e-ph couplings, and anharmonicity of phonons. Then we show our theoretical results in the Sec. III A summary given in Sec. IV.

## II. CRYSTAL STRUCTURES OF TETRACENE, RUBRENE, AND $C_{10}$ -DNBDT-NW

Figure 1 shows the structure of each OSC [26–28]. The molecular long axis of rubrene lies within the herringbone plane, while the molecular short axis of tetracene and  $C_{10}$ -DNBDT-NW lies within the herringbone plane. The space group of each OSC is  $P\bar{1}$ ,  $Cmca$ , and  $P2_1/c$  for tetracene, rubrene, and  $C_{10}$ -DNBDT-NW, respectively [26–28]. Transfer integrals between neighboring molecules within the herringbone plane are defined as shown in Fig. 1. The number of different kinds of transfer integrals between nearest neighbor sites is 4 in tetracene:  $t_{a1}$ ,  $t_{a2}$ ,  $t_{d1}$ , and  $t_{d2}$ , while it is 2 in rubrene ( $t_b$  and  $t_d$ ) and  $C_{10}$ -DNBDT-NW ( $t_c$  and  $t_d$ ), due to the difference in symmetry of the crystal structures. The maximum values of hole mobility previously reported in their FETs are  $2.4\text{ cm}^2/\text{V s}$  in tetracene [29],  $40\text{ cm}^2/\text{V s}$  in rubrene [3], and  $16\text{ cm}^2/\text{V s}$  in  $C_{10}$ -DNBDT-NW [4].

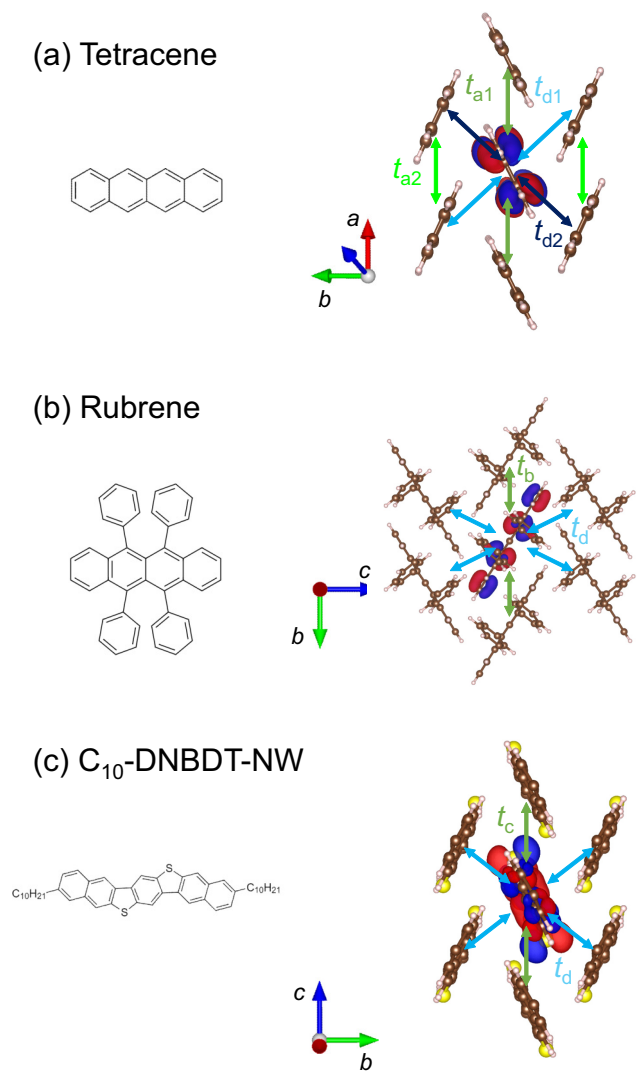


FIG. 1. Molecular structures and packing structures of (a) tetracene [26], (b) rubrene [27], and (c)  $C_{10}$ -DNBDT-NW [28] with maximally localized Wannier functions constructed from HOMO bands. The alkyl chains of  $C_{10}$ -DNBDT-NW are not shown for clarity.

Rubrene shows quasi-one-dimensional electric conduction [30], while tetracene and  $C_{10}$ -DNBDT-NW show two-dimensional ones [31,32].

## III. CALCULATION METHOD

### A. Normal mode analysis

To investigate low-frequency intermolecular vibrations or lattice phonons, we perform periodic boundary DFT calculations with CRYSTAL 17 code [33], which uses an all-electron Gaussian-type basis set. The B3LYP [34,35] exchange and correlation functional is employed with the 6-31G(d) basis set [36]. Grimme's  $D3$  dispersion correction is applied in order to treat London dispersion interactions [37].

First, the geometrical optimization is performed using the crystallographic data obtained experimentally [26–28]. The space group is fixed to an experimentally obtained one:  $P\bar{1}$  for

tetracene, *Cmca* for rubrene, and  $P2_1/c$  for  $C_{10}$ -DNBDT-NW. The calculations are performed with the primitive cell, which contains two molecules. The threshold energy is set to  $\Delta E < 10^{-10}$  hartree, and  $8 \times 8 \times 8$   $k$ -point samplings with  $\Gamma$ -centered  $k$  meshes are employed following the Monkhorst-Pack scheme [38].

Here, we detail the geometry optimization in rubrene. When the cell parameters are optimized, the lattice constants  $b$  and  $c$  of rubrene become smaller than those of the experimental structure at room temperature (2% and 5% underestimations, respectively). One of the causes for this underestimation is lack of thermal expansion in DFT calculations. In an x-ray diffraction study [27], the temperature dependence of the cell parameters are reported between 100 and 300 K in rubrene single crystals. The cell parameters are linearly decreased by lowering the temperature in this range. When we assume that the cell parameters are also linearly decreased from 100 to 0 K, the decreases in  $b$  and  $c$  by lowering the temperature from 300 to 0 K are estimated at 0.5% and 2%, respectively. Therefore, the cause of the underestimation is not only the lack of thermal expansion in the DFT calculations. These underestimations are not considered to be due to basis set superposition error (BSSE) because the underestimations of  $b$  and  $c$  also occur when the basis set is improved to pob-TZVP-rev2 [39] (3% and 6% underestimations, respectively). A most plausible reason is that the  $D3$  dispersion correction overestimates the intermolecular attractive force. Hence, we fix the cell parameters to the experimental values [26–28], which will give harmonic frequencies close to the experimental results.

After the cell-fixed geometry optimization,  $\Gamma$ -point vibrational frequency calculations [40,41] are performed with the same conditions. Mass-weighted dynamical matrix  $W(\mathbf{q} = \mathbf{0})$  takes the form

$$W_{i\alpha,j\beta}(\mathbf{q} = \mathbf{0}) = \frac{H_{i\alpha,j\beta}}{\sqrt{M_i M_j}}. \quad (1)$$

$M_i$  is the mass of the atom  $i$ , and  $H_{i\alpha,j\beta}$  is the second derivative of potential energy surface  $V(\mathbf{u})$  at equilibrium position with respect to a displacement of atom  $i$  in the  $\alpha$ -axis direction and a displacement of atom  $j$  in the  $\beta$ -axis direction:

$$H_{i\alpha,j\beta} = \left[ \frac{\partial^2 V(\mathbf{u})}{\partial u_{i\alpha} \partial u_{j\beta}} \right]_{\mathbf{u}=\mathbf{0}} \quad (i, j = 1, 2, \dots, N \quad \alpha, \beta = x, y, z), \quad (2)$$

where  $N$  is the number of atoms in a unit cell. The equilibrium structure corresponds to  $\mathbf{u} = \mathbf{0}$ . In the CRYSTAL code, the first derivative of  $V(\mathbf{u})$  with respect to the atomic displacement,  $v_{i\alpha} = \partial V / \partial u_{i\alpha}$ , is calculated analytically. Then mass-weighted dynamical matrix is numerically obtained via two-point formula:

$$\begin{aligned} W_{i\alpha,j\beta} &\approx W_{i\alpha,j\beta}^{(\text{num})} \\ &= \frac{1}{\sqrt{M_i M_j}} \frac{v_{i\alpha}(0, \dots, u_{i\alpha}, \dots) - v_{i\alpha}(0, \dots, 0, \dots)}{u_{i\alpha}}. \end{aligned} \quad (3)$$

We set the step size of displacement along each Cartesian axis  $u_{i\alpha} = 0.003 \text{ \AA}$ . The harmonic frequencies and the normal modes are defined by the following eigenvalue problem:

$$W \mathbf{e}_\lambda = \omega_\lambda^2 \mathbf{e}_\lambda. \quad (4)$$

$\mathbf{e}_\lambda$  is the unit eigenvector and  $\omega_\lambda$  is the harmonic frequency of the mode  $\lambda$ . The harmonic frequencies and the normal modes at the  $\Gamma$  point are computed by diagonalizing  $W^{(\text{num})}$ . We define the eigenvalue and the eigenvector of  $W^{(\text{num})}$  as  $[\omega_\lambda^{(1)}]^2$  and  $\mathbf{e}_\lambda^{(\text{num})}$ , respectively, in order to distinguish them from the exact results which do not include numerical errors. The relation between the unit eigenvector  $\mathbf{e}_\lambda^{(\text{num})}$  and the displacement of atom  $i$  of the phonon mode  $\lambda$  in the  $\alpha$ -axis direction  $u_{\lambda,i\alpha}^{(\text{num})}$  is given as follows:

$$u_{\lambda,i\alpha}^{(\text{num})} = \frac{e_{\lambda,i\alpha}^{(\text{num})}}{\sqrt{M_i}} Q_\lambda. \quad (5)$$

Here,  $Q_\lambda$  is the normal mode coordinate.

The normal mode analysis was the most time-consuming calculation. The time necessary for each calculation using Intel Xeon E5-2690v4 (2.6 GHz) was  $\sim 1$  day (27 cores) for tetracene,  $\sim 5$  days (27 cores) for rubrene, and  $\sim 25$  days (20 cores) for  $C_{10}$ -DNBDT-NW.

## B. Frequency correction

The frequency obtained by the above-mentioned method,  $\omega_\lambda^{(1)}$ , is affected by numerical errors, especially in the low-frequency region. In order to reduce the frequency errors, frequency correction is performed in the same way as reported in a previous study [13]. We calculate the increase in energy  $\Delta E_\lambda$  after changing the structure from  $\mathbf{u} = \mathbf{0}$  (optimized structure) to  $\mathbf{u} = \mathbf{u}_\lambda^{(\text{num})}$  for the given phonon mode  $\lambda$ . Then  $\Delta E_\lambda$  is fitted with a quadratic function with respect to the amplitude  $Q_\lambda$ :

$$\Delta E_\lambda(Q_\lambda) = \frac{1}{2} [\omega_\lambda^{(2)}]^2 Q_\lambda^2, \quad (6)$$

where  $\omega_\lambda^{(2)}$  is the corrected frequency. The corrected frequency  $\omega_\lambda^{(2)}$  is more accurate than  $\omega_\lambda^{(1)}$  (see the Appendix).

We apply the frequency correction only to low-frequency modes whose frequencies are smaller than the threshold frequency  $\omega_{\text{th}}$  since the relative error in the frequency tends to decrease with increase of the frequency. No frequency correction is applied to any phonon modes in tetracene because their calculated frequencies are sufficiently close to the experimental values. We set the threshold  $\omega_{\text{th}}$  to  $100 \text{ cm}^{-1}$  in rubrene and  $C_{10}$ -DNBDT-NW. In these OSCs, we confirmed that  $|\Delta\omega/\omega^{(2)}|$  is less than 10% for  $50 \text{ cm}^{-1} < \omega^{(2)} < 100 \text{ cm}^{-1}$ , which makes us expect that the numerical errors for  $\omega^{(2)} > 100 \text{ cm}^{-1}$  are not serious. We consider the scaling factor of B3LYP/6-31G(d) (0.96 [42]) additionally, and the resultant frequency  $\omega_\lambda^{(3)}$  becomes

$$\omega_\lambda^{(3)} = \begin{cases} 0.96 \omega_\lambda^{(2)} & (\text{for rubrene and } C_{10}\text{-DNBDT-NW, } \omega_\lambda^{(1)} < 100 \text{ cm}^{-1}) \\ 0.96 \omega_\lambda^{(1)} & (\text{otherwise}) \end{cases}. \quad (7)$$

Hereafter, we use  $\omega_\lambda^{(3)}$  for the calculations of the IR/Raman spectra and the nonlocal e-ph coupling constants.

### C. IR/Raman spectrum

In order to verify the validity of the calculations of vibrations, IR/Raman spectra in the low-frequency region are calculated. Imaginary part of the dielectric tensor is

$$\frac{\varepsilon_{2,jj}(\omega)}{\varepsilon_0} = \sum_\lambda \text{Im} \left\{ \frac{f_{jj,\lambda} [\omega_\lambda^{(3)}]^2}{[\omega_\lambda^{(3)}]^2 - \omega^2 - i\omega\gamma_\lambda} \right\}, \quad (8)$$

where  $jj$  indicates the polarization direction, and  $f_{jj,\lambda}$  and  $\gamma_\lambda$  are the oscillator strength and damping factor for the vibrational mode  $\lambda$ , respectively. The oscillator strength  $f_{jj,\lambda}$  is computed by the Berry phase method implemented in CRYSTAL code [43,44].

An intensity of polarized Raman scattering is described as

$$I_{\lambda,ij} \propto C \left( \frac{\partial \alpha_{ij}}{\partial Q_\lambda} \right)^2. \quad (9)$$

$$\begin{aligned} G_\lambda^{(0)} &= \frac{1}{3} \left( \frac{\partial \alpha_{xx}}{\partial Q_\lambda} + \frac{\partial \alpha_{yy}}{\partial Q_\lambda} + \frac{\partial \alpha_{zz}}{\partial Q_\lambda} \right)^2, \\ G_\lambda^{(1)} &= \frac{1}{2} \left[ \left( \frac{\partial \alpha_{xy}}{\partial Q_\lambda} - \frac{\partial \alpha_{yx}}{\partial Q_\lambda} \right)^2 + \left( \frac{\partial \alpha_{yz}}{\partial Q_\lambda} - \frac{\partial \alpha_{zy}}{\partial Q_\lambda} \right)^2 + \left( \frac{\partial \alpha_{zx}}{\partial Q_\lambda} - \frac{\partial \alpha_{xz}}{\partial Q_\lambda} \right)^2 \right], \\ G_\lambda^{(2)} &= \frac{1}{2} \left[ \left( \frac{\partial \alpha_{xy}}{\partial Q_\lambda} + \frac{\partial \alpha_{yx}}{\partial Q_\lambda} \right)^2 + \left( \frac{\partial \alpha_{yz}}{\partial Q_\lambda} + \frac{\partial \alpha_{zy}}{\partial Q_\lambda} \right)^2 + \left( \frac{\partial \alpha_{zx}}{\partial Q_\lambda} + \frac{\partial \alpha_{xz}}{\partial Q_\lambda} \right)^2 \right] + \frac{1}{3} \left[ \left( \frac{\partial \alpha_{xx}}{\partial Q_\lambda} - \frac{\partial \alpha_{yy}}{\partial Q_\lambda} \right)^2 + \left( \frac{\partial \alpha_{yy}}{\partial Q_\lambda} - \frac{\partial \alpha_{zz}}{\partial Q_\lambda} \right)^2 \right. \\ &\quad \left. + \left( \frac{\partial \alpha_{zz}}{\partial Q_\lambda} - \frac{\partial \alpha_{xx}}{\partial Q_\lambda} \right)^2 \right]. \end{aligned} \quad (12)$$

Raman spectra are calculated with the Coupled-Perturbed Kohn-Sham method implemented in CRYSTAL code [49,50].

### D. Transfer integral

Transfer integrals are calculated with MLWFs, which are constructed from Bloch functions consisting of the highest-occupied molecular orbital (HOMO) [14–16]. Because the unit cell contains two molecules, there are two HOMO-derived bands and two corresponding Bloch functions,  $\psi_{1k}(\mathbf{r})$  and  $\psi_{2k}(\mathbf{r})$ . The  $\alpha$  th Wannier function (WF) is defined as

$$w_{\alpha\mathbf{R}}(\mathbf{r}) = \frac{V_{\text{cell}}}{(2\pi)^3} \int_{\text{BZ}} d\mathbf{k} e^{-i\mathbf{k}\cdot\mathbf{R}} \sum_{\beta=1}^2 U_{\alpha\beta}^{(k)} \psi_{\beta k}(\mathbf{r}), \quad (13)$$

where  $\mathbf{R}$  is the lattice vector,  $V_{\text{cell}}$  is the volume of the unit cell, and  $U_{\alpha\beta}^{(k)}$  is a  $2 \times 2$  unitary matrix. MLWFs are defined as WFs where the unitary matrix  $U$  is set so as to minimize the localization functional  $\Omega$ :

$$\Omega = \sum_{\alpha=1}^2 [\langle w_{\alpha\mathbf{0}} | r^2 | w_{\alpha\mathbf{0}} \rangle - |\langle w_{\alpha\mathbf{0}} | \mathbf{r} | w_{\alpha\mathbf{0}} \rangle|^2]. \quad (14)$$

Although the WF is not necessarily localized in a molecule, the MLWF is localized in a molecule.

Here, the MLWF  $w_{\alpha\mathbf{0}}(\mathbf{r})$  is assumed to be localized at the molecule located at  $\delta_\alpha$ . The transfer integral between molecule  $N$  centered at  $\mathbf{r}_N = \mathbf{R}_N + \delta_{\alpha_N}$  and molecule  $M$  cen-

$i(j)$  indicates the polarization of incident (outgoing) light, and  $\alpha_{ij}$  is the polarizability tensor. The prefactor  $C$  depends on temperature  $T$  and the frequency of the incident light  $\omega_L$  as follows [45,46]:

$$C \sim \frac{[\omega_L - \omega_\lambda^{(3)}]^4}{30\omega_\lambda^{(3)}} \frac{1}{1 - \exp(-\frac{\hbar\omega_\lambda^{(3)}}{kT})}. \quad (10)$$

Unpolarized Raman intensities for a powder sample,  $I_{\lambda,\text{tot}}$ , can be calculated as [47,48]

$$I_{\lambda,\text{tot}} \propto C [10G_\lambda^{(0)} + 5G_\lambda^{(1)} + 7G_\lambda^{(2)}], \quad (11)$$

where  $G_\lambda^{(0)}$ ,  $G_\lambda^{(1)}$ , and  $G_\lambda^{(2)}$  are the rotation invariants:

tered at  $\mathbf{r}_M = \mathbf{R}_M + \delta_{\alpha_M}$  is obtained as

$$t_{MN} = \langle w_{\alpha_M \mathbf{R}_M} | \hat{H}_{\text{KS}} | w_{\alpha_N \mathbf{R}_N} \rangle, \quad (15)$$

where  $\hat{H}_{\text{KS}}$  is the Kohn-Sham Hamiltonian.

Here, we mention the difference between the MLWF method adopted here and the dimer projection (DIPRO) method [51,52]. The latter is a standard method to compute transfer integrals of OSCs. Strictly speaking, transfer integrals obtained by the DIPRO method are different from the exact tight binding parameters corresponding to HOMO-derived bands because a band consists of not only HOMOs but also other molecular orbitals such as second highest occupied molecular orbitals (SHOMOs). A transfer integral obtained using MLWFs is an effective value including the contribution from SHOMOs to HOMO-derived bands, which enlarges bandwidth in some OSCs such as [1] benzothieno[3,2-*b*] [1]benzothiophene (BTBT) based OSCs [53]. Previous research shows that the difference between computed transfer integrals of pentacene with the MLWF method and those with the DIPRO method is less than 10 meV, whereas e-ph coupling constants of pentacene obtained by the DIPRO method are slightly overestimated [16]. The transfer integrals calculated with MLWFs exactly correspond to tight binding parameters, and thus precise transfer integrals and nonlocal e-ph coupling constants can be obtained.



We calculate band structures, MLWFs, and transfer integrals using a plane-wave based code, XTAPP [54–56], in the optimized structures used in the vibrational calculations mentioned above. We adopt the norm-conserving pseudopotentials [56] and the Perdew–Burke–Ernzerhof (PBE) exchange–correlation functional [57,58], which is one of the generalized gradient approximation (GGA) functionals. The  $k$ -point samplings are done in  $5 \times 5 \times 3$  for tetracene and rubrene, and  $3 \times 3 \times 4$  for C<sub>10</sub>-DNBDT-NW with a  $\Gamma$ -centered grid. We confirmed that the changes in the values of the calculated transfer integrals are smaller than 0.2% when we varied the  $k$ -point sampling to  $6 \times 6 \times 3$  ( $3 \times 6 \times 6$ ) in tetracene and rubrene (C<sub>10</sub>-DNBDT-NW). The cutoff energy is set to 81 Ry for all the materials.

### E. Nonlocal e-ph coupling

Nonlocal e-ph couplings are introduced in a tight-binding Hamiltonian as follows:

$$\begin{aligned} \hat{H} &= \hat{H}_{\text{el}} + \hat{H}_{\text{e-ph}} + \hat{H}_{\text{ph}} \\ &= \sum_N \epsilon_N \hat{c}_N^\dagger \hat{c}_N + \sum_{M \neq N} \hat{t}_{MN} \hat{c}_M^\dagger \hat{c}_N \\ &\quad + \sum_{\lambda q} \hbar \omega_{\lambda q} \left( \hat{b}_{\lambda q}^\dagger \hat{b}_{\lambda q} + \frac{1}{2} \right). \end{aligned} \quad (16)$$

Here,  $\hat{H}_{\text{el}}$  ( $\hat{H}_{\text{ph}}$ ) is the electron (phonon) terms,  $\hat{H}_{\text{e-ph}}$  is the e-ph coupling terms,  $\hat{c}_N$  ( $\hat{c}_N^\dagger$ ) is the annihilation (creation) operator of an electron at the  $N$ th site with energy  $\epsilon_N$ , and  $\hat{b}_{\lambda q}$  ( $\hat{b}_{\lambda q}^\dagger$ ) is the annihilation (creation) operator of a phonon belonging to mode  $\lambda$  with wave vector  $\mathbf{q}$  and frequency  $\omega_{\lambda q}$ .  $\hat{t}_{MN}$  represents the transfer integral between  $N$ th site and  $M$ th site including e-ph coupling terms defined by

$$\begin{aligned} \hat{t}_{MN} &= t_{MN} + \frac{1}{\sqrt{N_\Omega}} \sum_{\lambda q} g_{\lambda MN}(\mathbf{q}) (\hat{b}_{\lambda q}^\dagger + \hat{b}_{\lambda, -q}) \\ &\equiv t_{MN} + \sum_{\lambda} \Delta \hat{t}_{\lambda MN}. \end{aligned} \quad (17)$$

$t_{MN}$  is the transfer integral of the equilibrium structure,  $N_\Omega$  is the number of unit cells,  $g_{\lambda MN}(\mathbf{q})$  is the e-ph coupling constant:

$$g_{\lambda MN}(\mathbf{q}) = \sqrt{\frac{\hbar}{2\omega_{\lambda q}}} \frac{\partial t_{MN}}{\partial Q_{\lambda q}}, \quad (18)$$

$$\langle (\Delta \hat{t}_{\lambda MN})^2 \rangle_T \approx \begin{cases} \frac{1}{2} [ |g_{\lambda MN}(\mathbf{0})|^2 + |g_{\lambda MN}(\frac{\pi}{a} \mathbf{e}_x)|^2 ] \coth\left(\frac{\hbar\omega_\lambda}{2kT}\right) & (\mathbf{r}_M = \mathbf{r}_N \pm a\mathbf{e}_x) \\ |g_{\lambda MN}(\mathbf{0})|^2 \coth\left(\frac{\hbar\omega_\lambda}{2kT}\right) & (\mathbf{r}_M = \mathbf{r}_N \pm \frac{a}{2}\mathbf{e}_x \pm \frac{b}{2}\mathbf{e}_y) \end{cases}. \quad (22)$$

The variance of the transfer integral between the nearest neighbor sites along the crystal axis is dominated by the frequencies of the  $\Gamma$ -point phonons and zone-edge phonons, which correspond to the in-phase vibrations and out-of-phase vibrations, respectively. The  $\Gamma$ -point approximation ignores the contribution from zone-edge optical phonons. Therefore, fluctuation of the transfer integral along the crystal axis is underestimated when we

and  $\Delta \hat{t}_{\lambda MN}$  is a transfer integral fluctuation by phonons belonging to mode  $\lambda$ . Hereafter, we only consider the transfer integral between nearest neighbor molecules. Considering a bulk system and taking the thermodynamic limit  $N_\Omega \rightarrow \infty$ , the variance of the transfer integral at temperature  $T$  is calculated as

$$\begin{aligned} \langle (\Delta \hat{t}_{MN})^2 \rangle_T &\equiv \langle (\hat{t}_{MN} - t)^2 \rangle_T \\ &= \sum_{\lambda} \langle (\Delta \hat{t}_{\lambda MN})^2 \rangle_T \\ &= \sum_{\lambda} \frac{V_{\text{cell}}}{(2\pi)^3} \int d\mathbf{q} |g_{\lambda MN}(\mathbf{q})|^2 \coth\left(\frac{\hbar\omega_{\lambda q}}{2kT}\right). \end{aligned} \quad (19)$$

$\langle \hat{O} \rangle_T$  is the thermal average value of an observable  $\hat{O}$  at temperature  $T$  defined as

$$\langle \hat{O} \rangle_T = \frac{\text{Tr}[\hat{O} \exp(-\frac{\hat{H}_{\text{ph}}}{kT})]}{\text{Tr}[\exp(-\frac{\hat{H}_{\text{ph}}}{kT})]}. \quad (20)$$

The transfer integral fluctuation  $\langle (\Delta \hat{t}_{MN})^2 \rangle_T$  is the key factor to compute the carrier mobility in a framework of the transient localization theory [10].

In our study, in order to avoid the high computational cost, we ignore the contributions of acoustic phonons to the transfer integral fluctuation. We compute e-ph couplings of only  $\Gamma$ -point phonons,  $g_{\lambda MN}(\mathbf{0})$ , and approximate those with wave vector  $\mathbf{q}$ ,  $g_{\lambda MN}(\mathbf{q})$ , using  $g_{\lambda MN}(\mathbf{0})$ . We call this treatment a  $\Gamma$ -point approximation. Here, we consider the meaning of this approximation. The  $\mathbf{q}$ -dependence of e-ph coupling constant  $g_{\lambda MN}(\mathbf{q})$  can be modeled as follows [59]:

$$\begin{aligned} g_{\lambda MN}(\mathbf{q}) &= \frac{1}{2} g_{\lambda MN}(\mathbf{0}) \sqrt{\frac{\omega_{\lambda 0}}{\omega_{\lambda q}}} (e^{i\mathbf{q} \cdot \mathbf{R}_M} + e^{i\mathbf{q} \cdot \mathbf{R}_N}) \\ &\quad + \frac{1}{2} g_{\lambda MN}(\mathbf{q}_{NM}) \sqrt{\frac{\omega_{\lambda q_{NM}}}{\omega_{\lambda q}}} e^{-i\mathbf{q}_{NM} \cdot \mathbf{R}_M} (e^{i\mathbf{q} \cdot \mathbf{R}_M} - e^{i\mathbf{q} \cdot \mathbf{R}_N}). \end{aligned} \quad (21)$$

In Eq. (21),  $\mathbf{q}_{NM} = \pi(\mathbf{R}_N - \mathbf{R}_M)/|\mathbf{R}_N - \mathbf{R}_M|^2$ . We neglect the  $\mathbf{q}$  dependence of the frequency of an optical phonon mode ( $\omega_{\lambda q} \approx \omega_{\lambda, q=0} \equiv \omega_\lambda$ ). When molecules form a herringbone structure on the  $xy$  plane,  $\langle (\Delta \hat{t}_{\lambda MN})^2 \rangle_T$  for the optical phonon mode is expressed as follows:

apply the  $\Gamma$ -point approximation. On the other hand, the variance of the transfer integral between the nearest neighbor sites along the diagonal axis can be calculated with the  $\Gamma$ -point e-ph coupling because the  $\Gamma$ -point phonon modes include both in-phase vibrations and out-of-phase vibrations.

We calculate the mode-resolved variance of transfer integral at room temperature from the  $\Gamma$ -point optical phonon

mode  $\sigma_{\lambda MN}^2$  defined as

$$\sigma_{\lambda MN}^2 \equiv |g_{\lambda MN}(\mathbf{0})|^2 \coth \left[ \frac{\hbar \omega_{\lambda}^{(3)}}{2kT} \right]. \quad (23)$$

The e-ph coupling constant  $g_{\lambda MN}(\mathbf{0})$  is computed via the central-difference approximation:

$$g_{\lambda MN}(\mathbf{0}) \approx \sqrt{\frac{\hbar}{2\omega_{\lambda}^{(3)}}} \frac{t_{MN}(\Delta Q_{\lambda, q=0}) - t_{MN}(-\Delta Q_{\lambda, q=0})}{2\Delta Q_{\lambda, q=0}}. \quad (24)$$

We set  $\Delta Q_{\lambda, q=0} = 0.1\sqrt{\hbar/\omega^{(1)}}$  for the numerical derivative.

### F. Anharmonicity of low-frequency phonons in C<sub>10</sub>-DNBDT-NW

According to the previous research [21], very low-frequency modes in alkylated OSCs show strong anharmonicity. Furthermore, as we discuss in the next section, we observe two imaginary frequency modes in C<sub>10</sub>-DNBDT-NW when fixing the space group as  $P2_1/c$ . Therefore, in C<sub>10</sub>-DNBDT-NW, anharmonicity of phonons should be taken into account. In order to estimate the anharmonic effects, the

$$\hat{H}_{\text{anharmon},\lambda} = \begin{cases} \hat{b}_{\lambda}^{\dagger} \hat{b}_{\lambda} + \frac{1}{2} + \frac{\alpha_{\lambda}}{2\sqrt{2}}(b_{\lambda} + b_{\lambda}^{\dagger})^3 + \frac{\beta_{\lambda}}{4}(b_{\lambda} + b_{\lambda}^{\dagger})^4 & (\text{for } \omega_{\lambda}^{(2)} : \text{real}) \\ -\frac{\hat{b}_{\lambda} \hat{b}_{\lambda} + \hat{b}_{\lambda}^{\dagger} \hat{b}_{\lambda}^{\dagger}}{2} + \frac{\alpha_{\lambda}}{2\sqrt{2}}(b_{\lambda} + b_{\lambda}^{\dagger})^3 + \frac{\beta_{\lambda}}{4}(b_{\lambda} + b_{\lambda}^{\dagger})^4 & (\text{for } \omega_{\lambda}^{(2)} : \text{imaginary}) \end{cases}. \quad (27)$$

By numerically diagonalizing the anharmonic Hamiltonian, the eigenstates  $|\phi_n\rangle$  and eigenenergies  $E_n$  are obtained. The amplitude of the anharmonic phonon  $\langle Q_{\lambda}^2 \rangle_{\text{anharmon},T}$  can be calculated as

$$\begin{aligned} \langle Q_{\lambda}^2 \rangle_{\text{anharmon},T} &= \frac{\text{Tr}[\hat{Q}_{\lambda}^2 \exp(-\frac{\hat{H}_{\text{anharmon},\lambda}}{kT})]}{\text{Tr}[\exp(-\frac{\hat{H}_{\text{anharmon},\lambda}}{kT})]} \\ &= \frac{\sum_n \langle \phi_n | \hat{Q}_{\lambda}^2 | \phi_n \rangle \exp(-\frac{E_n}{kT})}{\sum_n \exp(-\frac{E_n}{kT})}. \end{aligned} \quad (28)$$

We compute the mode-resolved transfer integral variance at room temperature from a  $\Gamma$ -point anharmonic phonon  $\sigma_{\lambda MN, \text{anharmon}}^2$  defined as

$$\sigma_{\lambda MN, \text{anharmon}}^2 = \left| \frac{\partial t_{MN}}{\partial Q_{\lambda}} \right|^2 \langle Q_{\lambda}^2 \rangle_{\text{anharmon},T}. \quad (29)$$

Note that this procedure only takes account of anharmonic terms proportional to  $Q_{\lambda, q=0}^3$  or  $Q_{\lambda, q=0}^4$ , while there are many more anharmonic terms, e.g., third order terms are generally described as  $\sum_{\lambda_1 q_1 \lambda_2 q_2 \lambda_3 q_3} \Phi_{\lambda_1 q_1 \lambda_2 q_2 \lambda_3 q_3} Q_{\lambda_1 q_1} Q_{\lambda_2 q_2} Q_{\lambda_3 q_3}$ . A methodology of calculating all the anharmonic coefficients and applying it to an inorganic material SrTiO<sub>3</sub> were reported [60]. However, the application of this method to OSCs requires a high computational cost due to the large number of atoms in a unit cell in OSCs. Therefore, we only consider  $Q_{\lambda, q=0}^3$  and  $Q_{\lambda, q=0}^4$  terms, which enables us to characterize the effect of anharmonicity.

potential curves of very low-frequency modes ( $<10 \text{ cm}^{-1}$ ) and the imaginary frequency modes are fitted with a quartic function and the Schrödinger equation of the one-dimensional anharmonic oscillator is solved. The Hamiltonian takes the form

$$\begin{aligned} \hat{H}_{\text{anharmon},\lambda} &= \frac{1}{2} \hat{P}_{\lambda}^2 + \frac{1}{2} [\omega_{\lambda}^{(2)}]^2 \hat{Q}_{\lambda}^2 + \alpha_{\lambda} \frac{|\omega_{\lambda}^{(2)}|^{5/2}}{\sqrt{\hbar}} \hat{Q}_{\lambda}^3 \\ &+ \beta_{\lambda} \frac{|\omega_{\lambda}^{(2)}|^3}{\hbar} \hat{Q}_{\lambda}^4, \end{aligned} \quad (25)$$

where  $\hat{P}_{\lambda}$  is the momentum operator which satisfies  $[\hat{Q}_{\lambda}, \hat{P}_{\lambda}] = i\hbar$ , and  $\alpha_{\lambda}$  and  $\beta_{\lambda}$  are the dimensionless anharmonic constants. We introduce annihilation (creation) operator  $b_{\lambda}$  ( $b_{\lambda}^{\dagger}$ ) as

$$\begin{aligned} \hat{b}_{\lambda} &= \sqrt{\frac{|\omega_{\lambda}^{(2)}|}{2\hbar}} \hat{Q}_{\lambda} + \frac{i}{\sqrt{2\hbar|\omega_{\lambda}^{(2)}|}} \hat{P}_{\lambda}, \\ \hat{b}_{\lambda}^{\dagger} &= \sqrt{\frac{|\omega_{\lambda}^{(2)}|}{2\hbar}} \hat{Q}_{\lambda} - \frac{i}{\sqrt{2\hbar|\omega_{\lambda}^{(2)}|}} \hat{P}_{\lambda}. \end{aligned} \quad (26)$$

Then, the Hamiltonian becomes

## IV. RESULTS AND DISCUSSIONS

### A. Frequency correction

We examine the influence of the frequency correction introduced in Sec. III B. Figure 2 shows an example of the frequency correction applied to the lowest frequency mode in C<sub>10</sub>-DNBDT-NW ( $\omega^{(1)} = 2.9 \text{ cm}^{-1}$ ). The broken line shows the change in energy,  $\Delta E = \frac{1}{2}(\omega^{(1)})^2 Q^2$ , as a

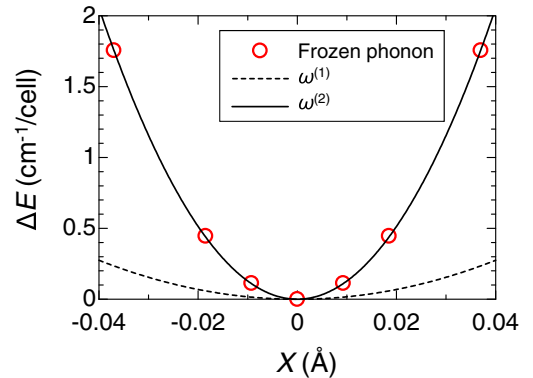


FIG. 2. The detail of the frequency correction applied to the lowest frequency modes of C<sub>10</sub>-DNBDT-NW ( $\omega^{(1)} = 2.9 \text{ cm}^{-1}$ ). The dashed line is  $\Delta E = \frac{1}{2}(\omega^{(1)})^2 Q^2$ , the red circles are DFT-calculated change in energy per cell, and the solid line is the fitting curve  $\Delta E = \frac{1}{2}(\omega^{(2)})^2 Q^2$ .

function of an atomic displacement  $X$  corresponding to a normal mode coordinate  $Q$ , which is defined by  $X = Q/\sqrt{M_{\text{tot}}}$  where  $M_{\text{tot}}$  is the total mass of the atoms in the unit cell. The open circles show the change in energy per cell obtained by the DFT-based calculation. The solid line is its fitting curve,  $\Delta E = \frac{1}{2}(\omega^{(2)})^2 Q^2$ . From this fitting, the corrected frequency  $\omega^{(2)} = 8.0 \text{ cm}^{-1}$  is obtained. The magnitude of frequency correction  $\Delta\omega \equiv \omega^{(2)} - \omega^{(1)}$  is  $5.1 \text{ cm}^{-1}$ .

We evaluate the magnitudes of frequency correction of the low-frequency modes  $\lambda$  ( $< 100 \text{ cm}^{-1}$ ),  $\Delta\omega_\lambda \equiv \omega_\lambda^{(2)} - \omega_\lambda^{(1)}$ , in rubrene as well as in C<sub>10</sub>-DNBDT-NW by performing the same procedures. The results of rubrene and C<sub>10</sub>-DNBDT-NW are shown in Figs. 3(a) and 3(b), respectively, in which not only  $\Delta\omega_\lambda$  but also its relative value  $\Delta\omega_\lambda/\omega_\lambda^{(2)}$  are presented. The maximum value of  $\Delta\omega_\lambda/\omega_\lambda^{(2)}$  is 11% for the mode with  $\omega_\lambda^{(2)} = 35 \text{ cm}^{-1}$  in rubrene and 63% for the mode with  $\omega_\lambda^{(2)} = 8 \text{ cm}^{-1}$  in C<sub>10</sub>-DNBDT-NW. The large value of  $\Delta\omega_\lambda/\omega_\lambda^{(2)}$  in C<sub>10</sub>-DNBDT-NW is probably related to the fact that this OSC has very low-frequency modes, and those modes are strongly affected by numerical errors. The results indicate that the frequency correction is important to estimate precisely amplitudes of thermally induced intermolecular vibrations in OSCs, especially when the mass of the constituent molecule is large. On the other hand, we do not apply the frequency correction to normal modes in tetracene because their calculated frequencies are very close to the experimental values, which is shown in Sec. III B.

### B. IR/Raman spectrum

In order to verify the reliability of the vibrational calculations presented above, we further calculate the IR/Raman spectra in the low-frequency region and compare the results with the spectra experimentally obtained. The symmetries of the normal modes and IR/Raman-active polarization directions are summarized in Table I. Here, we calculate the unpolarized Raman spectrum in tetracene, the polarized Raman and IR spectra in rubrene, and the polarized Raman spectra in C<sub>10</sub>-DNBDT-NW. Some of those spectra were experimentally obtained [61–63]. The polarized Raman spectra of C<sub>10</sub>-DNBDT-NW are measured in the present study.

In the Raman spectroscopy of C<sub>10</sub>-DNBDT-NW, a Horiba LabRAM HR Evolution spectrometer equipped with an optical microscope and a He-Ne laser (633 nm) was used. The polarization of the incident light was controlled via a half-wave plate. A polarizer was set to select the polarization of the detected scattered light. The spectra were measured in the backscattering geometry.

#### 1. Raman spectrum in tetracene

In Fig. 4, the solid line shows the unpolarized Raman spectrum of a powder sample of tetracene at 298 K experimentally obtained in the previous study [61]. The wavelength of the incident light is 752.5 nm. The broken line shows the calculated spectrum obtained in the present study, in which the full width at half maximum is set to  $8 \text{ cm}^{-1}$  in all the

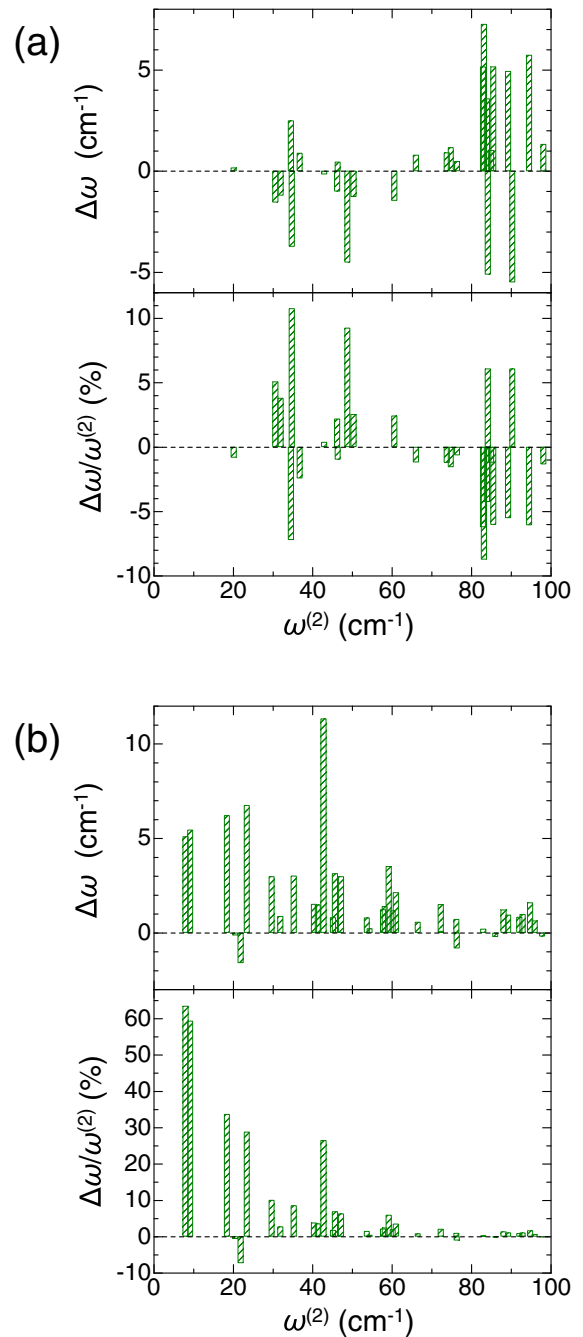


FIG. 3. The results of the frequency correction to (a) rubrene and (b) C<sub>10</sub>-DNBDT-NW.

modes in common. The calculated spectrum well reproduces the frequency and relative intensity of each Raman band ( $A_g$  mode) in the experimental spectrum. The root-mean-square deviation (RMSD) of the frequencies calculated in our study from the frequencies experimentally obtained in the range of  $20 \text{ cm}^{-1} < \omega^{(3)} < 150 \text{ cm}^{-1}$  is  $1.9 \text{ cm}^{-1}$ , which is much smaller than that ( $\sim 8.0 \text{ cm}^{-1}$ ) of the frequencies evaluated by the quasiharmonic lattice dynamics calculations [61]. It also much smaller than RMSDs in the other OSCs as described below.

TABLE I. List of IR/Raman-active polarization directions in tetracene, rubrene and C<sub>10</sub>-DNBDT-NW.

	Symmetry	IR	Raman
Tetracene	A <sub>g</sub>	inactive	all
	A <sub>u</sub>	all	inactive
Rubrene	A <sub>g</sub>	inactive	xx, yy, zz
	B <sub>1g</sub>	inactive	xy
	B <sub>2g</sub>	inactive	xz
	B <sub>3g</sub>	inactive	yz
	A <sub>u</sub>	inactive	inactive
	B <sub>1u</sub>	z	inactive
	B <sub>2u</sub>	y	inactive
C <sub>10</sub> -DNBDT-NW	B <sub>3u</sub>	x	inactive
	A <sub>g</sub>	inactive	xx, yy, zz, xz
	B <sub>g</sub>	inactive	xy, yz
	A <sub>u</sub>	y	inactive
	B <sub>u</sub>	x, z	inactive

## 2. Polarized Raman and absorption spectra in rubrene

Figures 5(a) and 5(b) show the experimental polarized Raman spectra in rubrene crystals previously reported at room temperature [62] and the corresponding spectra calculated in the present study, respectively. The wavelength of the incident light is 647.1 nm. The direction of electric fields of the incident light is parallel to the *b* axis and that of the scattering light is parallel to the *b* or *c* axis as shown in the upper panel. In two configurations, the peaks observed in the experiments are almost reproduced in the calculations, while the relative intensities of the peaks at 35, 105, and 120 cm<sup>-1</sup> and peak positions of the peaks at 35 and 75 cm<sup>-1</sup> are slightly deviated. RMSD of peak frequencies evaluated using the experimental spectrum in the range of 20 cm<sup>-1</sup> < ω<sup>(3)</sup> < 200 cm<sup>-1</sup> is 6.5 cm<sup>-1</sup>.

Figure 6(a) shows the spectra of imaginary part of dielectric constants, ε<sub>2</sub>, in the terahertz (THz) region in a rubrene single crystal. The electric fields of lights are parallel to the *b* or *c* axis. Those spectra were measured at 294 K

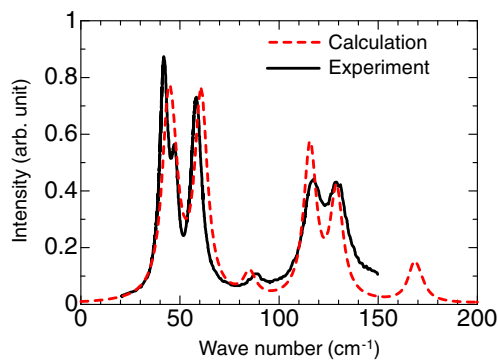


FIG. 4. Comparison of an experimental unpolarized Raman spectrum of tetracene (the black solid line) taken from Ref. [61] and a calculated one (the red broken line) at room temperature. The wavelength of the incident light is 752.5 nm. The calculated Raman peaks were convolved using Lorentzian line shapes with a full width at half-maximum (FWHM) of 8 cm<sup>-1</sup>.

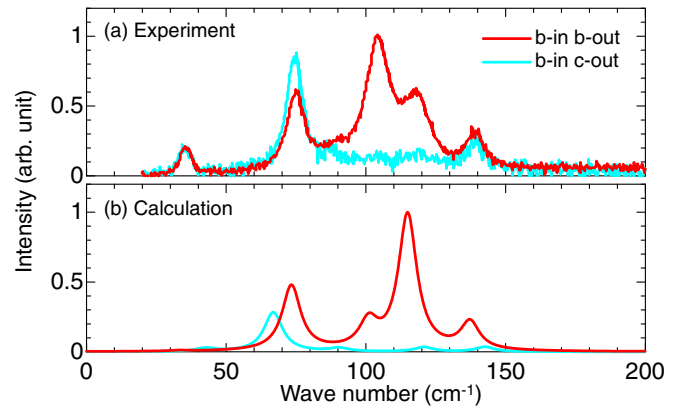


FIG. 5. Comparison of (a) experimental polarized Raman spectra of rubrene taken from Ref. [62] and (b) calculated ones at room temperature. The wavelength of the incident light is 647.1 nm. The calculated Raman peaks were convolved using Lorentzian line shapes with a FWHM of 8 cm<sup>-1</sup>.

using the THz time-domain spectroscopy (THz-TDS) and reported previously by some of the authors in this paper [61]. Figure 6(b) shows the calculated ε<sub>2</sub> spectra, which reproduce well both the frequency and oscillator strength of each band experimentally obtained. RMSD of peak frequencies evaluated using the experimental spectrum in the range of 40 cm<sup>-1</sup> < ω<sup>(3)</sup> < 350 cm<sup>-1</sup> is 7.4 cm<sup>-1</sup>.

While the computed Raman spectra are somewhat different from the experimental ones, the computed IR spectra well reproduce the experimental ones. Therefore, we consider that the computed normal modes in rubrene are reliable.

## 3. Polarized Raman spectra in C<sub>10</sub>-DNBDT-NW

Figures 7(a) and 7(b) show the experimental polarized Raman spectra in C<sub>10</sub>-DNBDT-NW single crystals at room temperature and the corresponding calculated spectra. The wavelength of the incident light is 633 nm. The directions of electric fields of the incident and scattering lights are parallel

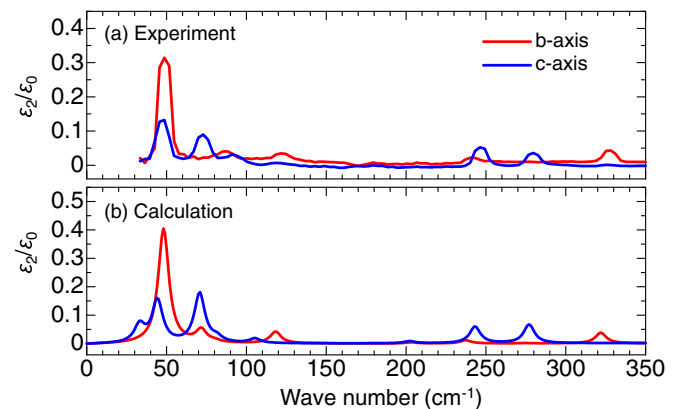


FIG. 6. Comparison of (a) experimental polarized ε<sub>2</sub> spectra of Rubrene taken from Ref. [63] and (b) calculated ones at room temperature. The red and blue lines show the spectra with the electric fields of lights parallel to the *b* and *c* axis, respectively. In the calculated spectra, γ<sub>λ</sub> is set to 8 cm<sup>-1</sup>.



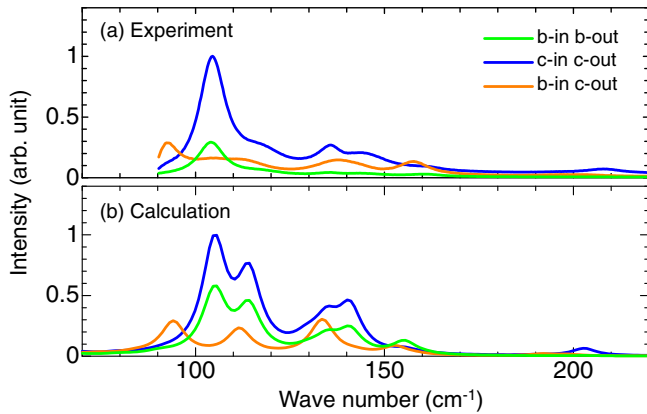


FIG. 7. Comparison of (a) experimental polarized Raman spectra of  $C_{10}$ -DNBDT-NW and (b) calculated ones at room temperature. The wavelength of the incident light is 633 nm. The calculated Raman peaks were convolved using Lorentzian line shapes with a FWHM of  $8 \text{ cm}^{-1}$ .

to the  $b$  or  $c$  axis as shown in the upper panel. The overall features of the experimental spectra are almost reproduced by the calculated ones, although the relative intensity of each band in the calculated spectra is not completely the same as those in the experimental spectra. The RMSD of peak frequencies evaluated using the experimental spectrum in the range of  $90 \text{ cm}^{-1} < \omega^{(3)} < 220 \text{ cm}^{-1}$  is  $4.1 \text{ cm}^{-1}$ .

Combining the comparisons of the IR/Raman spectra in the three OSCs, we can consider that our vibrational calculations are reliable.

### C. Transfer integral

As mentioned in Sec. III C, we calculate transfer integrals using MLWFs. First, we calculate the MLWFs using the Bloch functions of the HOMO-derived bands in the region of  $-1.2 \text{ eV} < E < -0.6 \text{ eV}$  and obtain the band dispersions by taking into account all the transfer integrals between two molecules far from each other, which is called Wannier interpolated bands. In Fig. 8, we show by the red solid lines the band dispersions of  $C_{10}$ -DNBDT-NW thus obtained, which are completely the same as those obtained using the PBE exchange-correlation functional shown by the solid black lines. These results support the validity of the MLWFs obtained in our framework. The MLWFs for tetracene and rubrene are computed in the same way. The obtained MLWFs in tetracene, rubrene, and  $C_{10}$ -DNBDT-NW are visualized in Fig. 1. Each MLWF is localized in a molecule, which is one of the conditions to treat MLWFs as the basis of a tight binding model. The results of Wannier interpolated bands and visualized MLWF show that the construction of tight binding model corresponding to HOMO-derived bands is successful (see Fig. 8). The tight binding parameters computed using these MLWFs are listed at Table II. The calculated transfer integrals are consistent with those reported in the previous studies [4,64], in which the dimer projection method (DIPRO) [51,52] and the experimentally determined structure were used [4,26,27]. Note that there are many previous studies that report the transfer integral of rubrene [10,13,16,20–23,65],

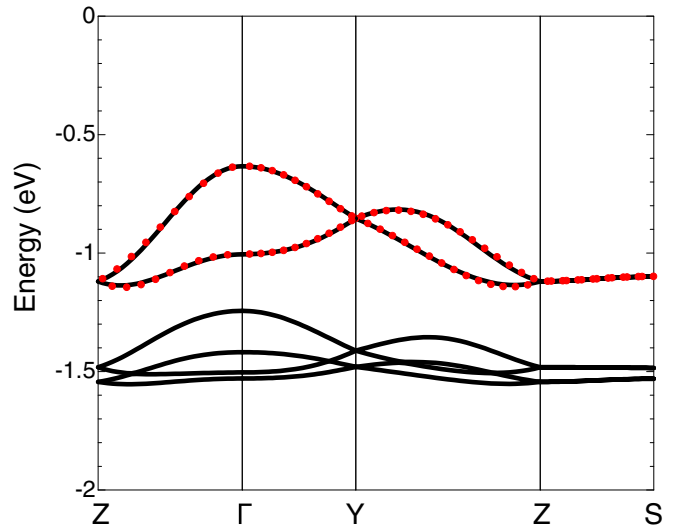


FIG. 8. PBE band structure (black solid lines) and Wannier interpolated bands (red dotted lines) of  $C_{10}$ -DNBDT-NW. The band dispersions are plotted along the high-symmetry points where  $\Gamma = (0,0,0)$ ,  $Y = (0,1/2,0)$ ,  $Z = (0,0,1/2)$ ,  $S = (0,1/2,1/2)$ . The zero of energy is the fermi level.

and a variety of values of  $t_b$  are reported ( $85 \text{ meV} \leq t_b \leq 145 \text{ meV}$ ). A possible origin for such variations is the difference in the structures used in the calculations, e.g., an experimentally obtained structure or an optimized structure. The difference of functional used for the calculations of transfer integrals may also cause the variations. It was reported that a transfer integral derived by the DFT calculation linearly increases with the amount of Hartree-Fock (HF) exchange in rubrene [65]. The amount of HF exchange is 0% in the PBE functional, so that our calculated transfer integral  $t_b$  is relatively small.

### D. Fluctuation of transfer integral without anharmonicity

The low-frequency nonlocal e-ph coupling constants  $g_{\lambda MN}(\mathbf{0})$  are obtained by the numerical derivatives of transfer integrals computed with the MLWFs as detailed in Sec. III E.

TABLE II. Tight binding parameters of HOMO-derived bands for tetracene, rubrene, and  $C_{10}$ -DNBDT-NW (in meV).  $\Delta\epsilon$  is the on-site energy difference between two molecules in a unit cell.

		This work	Reference [4,64]
Tetracene	$t_{a1}$	10.77	16
	$t_{a2}$	-5.75	-4
	$t_{d1}$	68.34	70
	$t_{d2}$	-20.61	-23
	$\Delta\epsilon$	8.81	
	Rubrene	$t_b$	76.91
$t_d$		16.02	15
$\Delta\epsilon$		0	
$C_{10}$ -DNBDT-NW	$t_c$	68.09	51
	$t_d$	44.80	50
	$\Delta\epsilon$	0	

TABLE III. Calculated harmonic frequencies and e-ph couplings in tetracene.

Symmetry	$\omega_\lambda^{(3)}$ (cm <sup>-1</sup> )	$g_{a1}$ (meV)	$g_{a2}$ (meV)	$g_{d1}$ (meV)	$g_{d2}$ (meV)
$A_g$	43.9	3.3	3.0	0.03	-0.4
	46.5	3.5	-2.1	-1.8	-1.9
	60.7	-0.7	2.4	0.9	-2.1
	85.1	0.5	0.6	-0.9	0.4
	115.6	-0.4	-0.6	2.7	0.9
	129.0	-0.9	0.1	-6.2	-2.4
	168.2	-0.1	-0.2	-0.3	0.02
	171.6	0.4	-0.2	-0.3	-0.9
	210.4	0.6	0.6	0.9	0.1
	215.7	0.7	-0.2	-1.7	-2.1
$A_u$	32.1	0	0	-2.0	4.0
	66.2	0	0	0.1	-0.5
	70.1	0	0	-0.2	1.6
	96.4	0	0	-4.5	-1.6
	103.9	0	0	-2.5	-1.8
	136.8	0	0	-0.5	1.0
	146.7	0	0	-0.7	-2.1
	163.4	0	0	0.7	0.9
	168.2	0	0	-0.2	-0.8

The values of  $g_{\lambda MN}(\mathbf{0})$  are shown in Tables III–V for tetracene, rubrene, and C<sub>10</sub>-DNBDT-NW, respectively. We also calculate the mode-resolved variance of transfer integral  $\sigma_{\lambda MN}^2$  at 293 K and investigate the important normal modes having large  $\sigma_{\lambda MN}^2$ , which is one of the main topics of the present study.

Before the discussion about the identifications of the important normal modes, we mention the relation between the

symmetry of phonons and the e-ph coupling constants. Some of e-ph coupling constants become zero from symmetry:  $g_{a1} = g_{a2} = 0$  for  $A_u$  modes in tetracene,  $g_b = 0$  for  $B_{1g}$ ,  $B_{2g}$ ,  $A_u$ ,  $B_{1u}$ ,  $B_{2u}$ , and  $B_{3u}$  modes in rubrene,  $g_d = 0$  for  $B_{1g}$ ,  $B_{2g}$ ,  $A_u$ , and  $B_{3u}$  modes in rubrene, and  $g_c = 0$  for  $A_u$  and  $B_u$  modes in C<sub>10</sub>-DNBDT-NW.

Figure 9 shows the mode-resolved variances of the transfer integrals  $\sigma_{\lambda a1}^2$ ,  $\sigma_{\lambda a2}^2$ ,  $\sigma_{\lambda d1}^2$ , and  $\sigma_{\lambda d2}^2$  in tetracene, and Fig. 10

TABLE IV. Calculated harmonic frequencies and e-ph couplings in rubrene.

Symmetry	$\omega_\lambda^{(3)}$ (cm <sup>-1</sup> )	$g_b$ (meV)	$g_d$ (meV)	$\omega_\lambda^{(3)}$ (cm <sup>-1</sup> )	$g_b$ (meV)	$g_d$ (meV)
$A_g$	33.2	-1.8	0.04	114.9	-1.6	0.4
	73.3	-4.2	1.1	137.3	1.4	0.04
	101.0	-1.3	0.4			
$B_{1g}$	30.7	0	0	103.4	0	0
	42.3	0	0	123.7	0	0
	82.1	0	0	161.9	0	0
$B_{2g}$	29.4	0	0	94.2	0	0
	58.2	0	0	130.1	0	0
	79.6	0	0	158.5	0	0
$B_{3g}$	41.2	1.9	-0.5	116.0	-0.6	0.3
	63.4	-4.8	0.4	136.9	-1.7	-1.1
	79.8	0.7	0.2			
$A_u$	19.4	0	0	90.8	0	0
	44.3	0	0	110.5	0	0
	86.7	0	0	168.5	0	0
$B_{1u}$	33.4	0	-0.2	81.6	0	-1.0
	44.5	0	0.7	105.5	0	-0.5
	70.9	0	-0.3			
$B_{2u}$	46.8	0	-0.7	80.6	0	-0.6
	48.3	0	-0.8	118.4	0	-0.6
	71.8	0	0.3			
$B_{3u}$	35.3	0	0	131.1	0	0
	80.8	0	0	165.7	0	0
	85.7	0	0			

TABLE V. Calculated harmonic frequencies and e-ph couplings in C<sub>10</sub>-DNBDT-NW.

Symmetry	$\omega_{\lambda}^{(3)}$ (cm <sup>-1</sup> )	$g_c$ (meV)	$g_d$ (meV)	$\omega_{\lambda}^{(3)}$ (cm <sup>-1</sup> )	$g_c$ (meV)	$g_d$ (meV)	
A <sub>g</sub>	21.0	0.8	-0.6	105.0	-0.07	-1.2	
	22.5	0.03	0.03	114.1	0.3	-0.8	
	41.1	-0.6	0.2	128.3	-0.1	-0.04	
	43.8	0.1	-0.2	130	0.06	0.008	
	56.8	-0.008	-0.009	134.7	-0.5	-0.3	
	58.6	-0.2	-0.04	140.8	-0.4	0.3	
	69.5	-0.4	0.09	155.2	0.7	-0.2	
	79.7	-0.2	0.3	160.1	-0.6	0.3	
	91.0	-0.06	-0.2	163.9	-0.07	0.03	
	92.1	0.09	-0.3	190.6	0.4	-0.3	
	B <sub>g</sub>	8.8	-0.3	1.5	111.6	0.4	-0.3
		30.6	0.5	-0.4	125.2	-0.05	-0.2
		39.7	0.4	0.2	130.2	-0.07	-0.1
		51.5	-0.4	-0.04	133.6	0.42	-0.9
55.9		0.06	-0.09	142.2	-0.08	-0.9	
57.8		-0.3	-0.3	152.8	0.9	0.9	
73.2		0.4	0.2	158.3	0.4	0.5	
84.6		-0.08	0.5	163.9	0.04	0.009	
89.2		0.1	0.4	191.9	0.2	0.2	
93.9		0.3	-0.6	198.4	-0.2	0.2	
A <sub>u</sub>		7.7	0	-3.0	108.6	0	-0.5
		19.7	0	1.3	123.1	0	0.2
		33.9	0	0.08	126.0	0	-0.4
		38.8	0	0.7	131.5	0	-1.2
	43.3	0	0.7	133.1	0	0.2	
	52.2	0	-1.1	156.3	0	0.2	
	63.8	0	-1.0	164.5	0	0.01	
	73.2	0	0.3	167.5	0	-1.3	
	82.6	0	0.3	176.0	0	1.6	
	88.4	0	0.04				
	B <sub>u</sub>	17.7	0	0.04	116.4	0	0.2
		28.5	0	0.04	124.4	0	0.04
		36.0	0	-0.01	125.4	0	0.1
		45.3	0	-0.09	129.2	0	0.1
55.4		0	-0.12	132.9	0	-0.1	
65.7		0	0.5	155.2	0	1.0	
69.4		0	-0.3	157.8	0	-0.1	
85.7		0	-0.06	164.4	0	0.1	
92.4		0	-0.6	177.9	0	0.7	
100.2		0	-2.1				

shows the normal modes  $A$ – $F$  which strongly fluctuate the transfer integrals. As seen in Fig. 10, except for mode  $E$ , these modes are simple intermolecular vibrational modes. In mode  $E$ , the intermolecular translation is mixed with the molecular bending.

The fluctuations of the transfer integrals,  $\Delta t_{MN}$ , in tetracene calculated with the e-ph coupling constants obtained in our study (in Ref. [18]) based on the  $\Gamma$ -point approximation are 10 meV (15 meV) for  $\Delta t_{d1}$ , 9.1 meV (13 meV) for  $\Delta t_{a2}$ , 19 meV (25 meV) for  $\Delta t_{d1}$ , and 19 meV (26 meV) for  $\Delta t_{d2}$ . The values of  $\Delta t_{MN}$  computed in tetracene are almost the same as those computed in the previous study.

Figure 11(a) shows the mode-resolved variances of the transfer integrals  $\sigma_{\lambda b}^2$  and  $\sigma_{\lambda d}^2$  in rubrene. Here, we focus only on the variances of transfer integral  $t_b$ ,  $\sigma_{\lambda b}^2$ , because rubrene shows quasi-one-dimensional electric conduction along the  $b$  axis. In fact, it is ascertained that  $\sigma_{\lambda b}^2$  is larger than  $\sigma_{\lambda d}^2$ . The

upper panel of Fig. 11(a) shows that the normal modes  $G$  and  $H$  strongly fluctuate  $t_b$ . These two modes are schematically shown in Fig. 11(b). They are both intermolecular libration within the herringbone plane. The strong e-ph coupling of these modes are consistent with the previous studies [20,63].

$\Delta t_b$  and  $\Delta t_d$  in rubrene at 293 K calculated with the e-ph coupling constants in our study are 13 and 6.4 meV, respectively.  $\Delta t_b$  calculated using e-ph coupling constants in Ref. [20] reaches 23 meV. Although the  $\Delta t_b$  value evaluated in our study is about half of that reported in the previous study, the  $\Delta t_b/t_b$  values evaluated in two studies are almost the same with each other: 17% in our study and 18% in Ref. [20]. On the other hand, the reported values of  $\Delta t_b/t_b$  at room temperature in Refs. [17,23] are much larger (48% and 33%, respectively), in which a supercell approach was used to sample the  $\mathbf{q}$  points other than the  $\Gamma$  point. This difference implies that the  $\Gamma$ -point approximation causes an

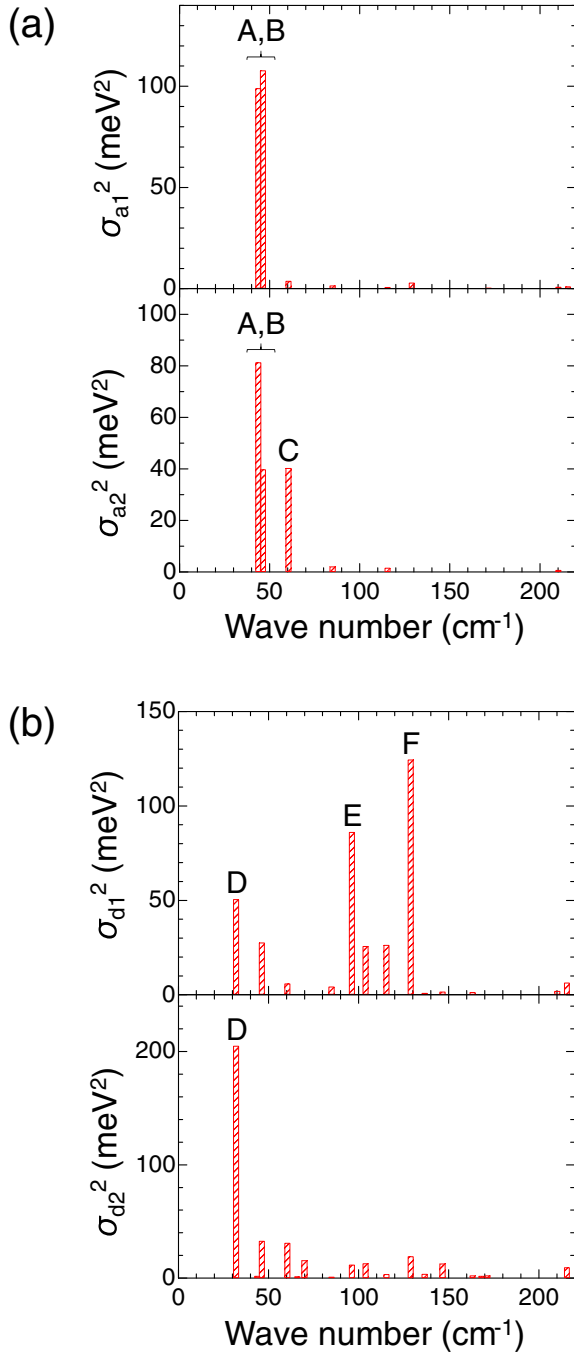


FIG. 9. Mode-resolved variances of transfer integrals induced by thermally excited phonon  $\sigma_{\lambda MN}^2$  at room temperature in tetracene. (a)  $\sigma_{a1}^2$ ,  $\sigma_{a2}^2$ . (b)  $\sigma_{d1}^2$ ,  $\sigma_{d2}^2$ .

underestimation of  $\Delta t_b/t_b$  due to the lack of the contribution of the zone-boundary optical phonons and acoustic phonons.

Figure 12(a) shows the mode-resolved variances of the transfer integrals  $\sigma_{\lambda c}^2$  and  $\sigma_{\lambda d}^2$  in C<sub>10</sub>-DNBDT-NW.  $\sigma_{\lambda d}^2$  of the normal modes I–K are especially large among all of  $\sigma_{\lambda c}^2$  and  $\sigma_{\lambda d}^2$ . Those three modes are schematically illustrated in Fig. 12(b). In mode I, the molecule is translated along the long molecular axis. Mode K resembles mode I except for the motions of the alkyl chains. The alkyl chains are deformed in mode K, while they are not in mode I. Mode J is an inter-

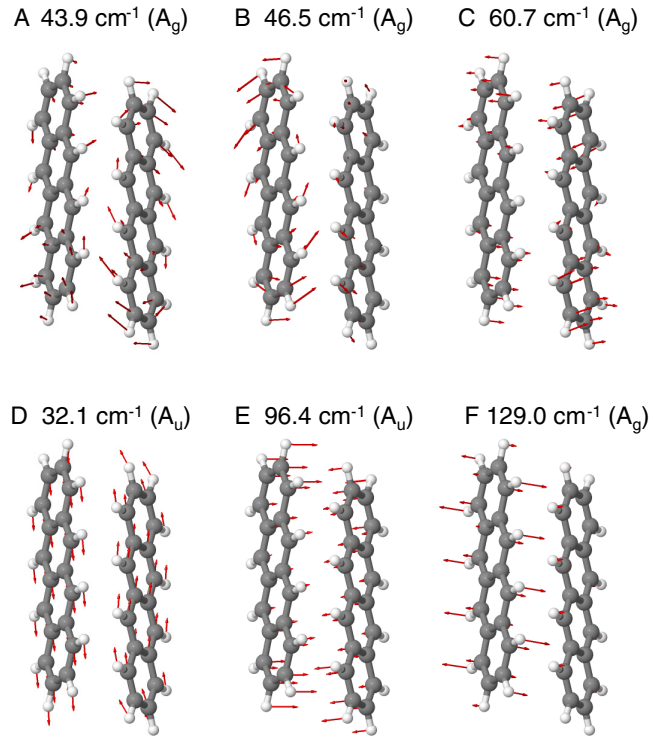


FIG. 10. Atomic displacements of normal modes A–F in tetracene.

molecular libration mode. A previous study reported that the frequency of modes I and J are 16.3 and 15.2 cm<sup>−1</sup>, respectively [25], whereas our calculation gives the frequencies of 7.7 and 8.8 cm<sup>−1</sup>, respectively. Although the absolute values of frequencies are somewhat different, both results suggest that the low-frequency modes play significant roles in the scatterings of carriers suppressing the mobility.

Mode I has the largest  $\sigma_{\lambda d}^2$  value, that is consistent with the previous calculation [25]. Our results show that the total contribution of the  $\Gamma$ -point phonons including mode I to the fluctuation of  $t_d$  is 60% of the original value ( $\frac{\sqrt{\sum_{\lambda} \sigma_{\lambda d}^2}}{t_d} = 60\%$ ), and that mode I contributes 81% to the total variance of  $t_d$  ( $\frac{\sigma_{\lambda=I,d}}{\sqrt{\sum_{\lambda} \sigma_{\lambda d}^2}} = 81\%$ ). Therefore, the fluctuation of mode I should be one of the main factors to suppress carrier mobility. This prediction, where the very low-frequency mode I ( $\omega = 7.7$  cm<sup>−1</sup> = 11 K) limits the mobility, is consistent with a temperature  $T$  dependence of spin-lattice relaxation time  $T_1$  obtained from electron spin resonance spectroscopy, where the relation between  $T_1$  and  $T$  does not change in the range from 10 to 300 K ( $T_1 \propto T^{-2.85}$ ) [6]. A similar result has been reported for C<sub>8</sub>-DNNT, whose thermally induced translation along the long molecular axis contributes the most to the total fluctuation of the transfer integral [21]. Our results also show that the fluctuation of  $t_c$  is small ( $\frac{\sqrt{\sum_{\lambda} \sigma_{\lambda c}^2}}{\sqrt{2}t_c} = 6\%$ ) under the  $\Gamma$ -point approximation in C<sub>10</sub>-DNBDT-NW. Another previous study [10] using a molecular dynamics simulation shows that the fluctuation of  $t_d$  is 58%, which is in good agreement with our result (60%). On the other hand, the study shows that the fluctuation of  $t_c$  reaches 38% [10], which is larger than our result (6%). Considering that our calculations neglect



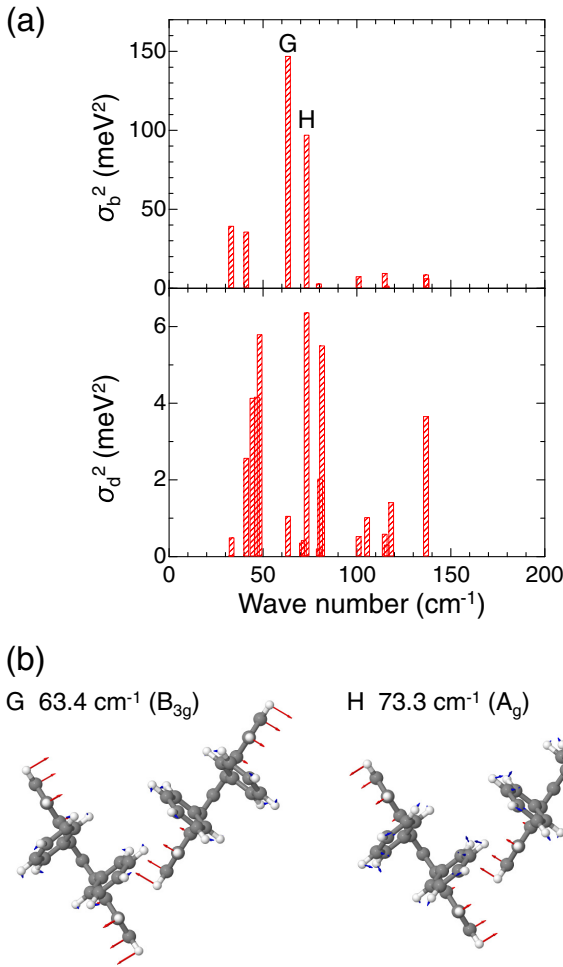


FIG. 11. (a) Mode-resolved variances of transfer integrals induced by thermally excited phonon  $\sigma_{\lambda b}^2$  and  $\sigma_{\lambda d}^2$  at room temperature in rubrene. (b) Atomic displacements of normal modes  $G$  and  $H$ . The atomic displacements in phenyl side groups are denoted by blue arrows.

the contributions of the zone-edge phonons and the previous molecular dynamics simulation includes the contributions from all the wave vectors of phonons, the zone-edge phonons ( $q_z = \pi/c$ ) are likely to contribute strongly to the fluctuation of  $t_c$ .

### E. Anharmonicity of phonons in C<sub>10</sub>-DNBDT-NW

In this section, we discuss the anharmonicity of the very low-frequency modes,  $I$  and  $J$ , and imaginary frequency modes,  $L$  and  $M$  (see Fig. 13). Figure 14 shows the potential curves of these modes and the fitting curves with quartic functions. These potential curves are even functions. This means that the symmetry of these modes is not  $A_g$ , and the symmetry of the crystal structure after displacing atoms along the normal mode coordinate is lower than that of the equilibrium crystal structure. Therefore, the dimensionless anharmonic constant for the third-order term  $\alpha_\lambda$  in Eq. (25) becomes zero. The anharmonic constant for the fourth-order term,  $\beta_\lambda$ , and the mode-resolved transfer integral variances,  $\sigma_{\lambda c, \text{anharmon}}^2$  and  $\sigma_{\lambda d, \text{anharmon}}^2$ , are listed in Table VI. The mode-resolved variances of transfer integrals with harmonic approximation,

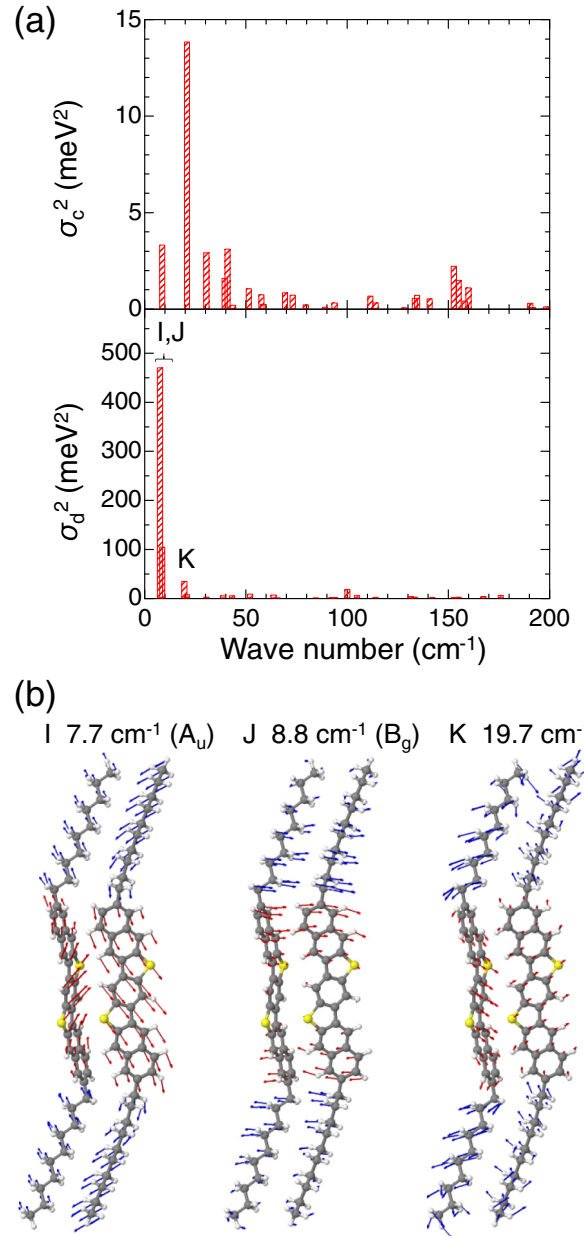


FIG. 12. (a) Mode-resolved variances of transfer integrals induced by thermally excited phonon  $\sigma_{\lambda c}^2$  and  $\sigma_{\lambda d}^2$  at room temperature in C<sub>10</sub>-DNBDT-NW. (b) Atomic displacements of normal modes  $I$ – $K$ . The atomic displacements in alkyl chains are denoted by blue arrows.

$\sigma_{\lambda c, \text{harm}}^2$  and  $\sigma_{\lambda d, \text{harm}}^2$ , are also listed for comparison.  $\sigma_{\lambda c, \text{anharmon}}^2$  and  $\sigma_{\lambda d, \text{anharmon}}^2$  for the imaginary frequency modes are small enough to ignore although imaginary frequency modes give infinite contributions of transfer integral fluctuations within the harmonic approximation. It is because thermal vibrations of these modes are suppressed due to the strong anharmonicity. The mode-resolved variances of all transfer integrals for modes  $I$  and  $J$  decrease to 36% and 39% of those computed with harmonic approximation, respectively. The total amount of the transfer integral fluctuation for  $t_d$  reaches  $0.42t_d$  when we consider the anharmonicity of  $I$ ,  $J$ ,  $L$ , and  $M$ , while it

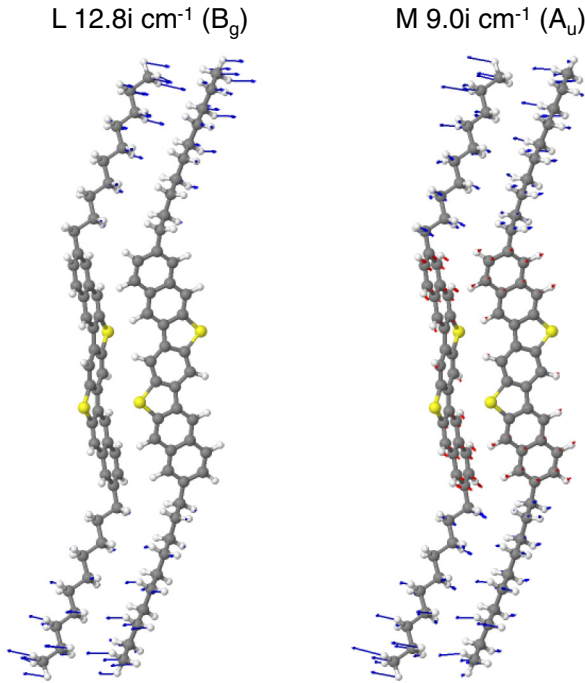


FIG. 13. Atomic displacements of two imaginary frequency modes in  $C_{10}$ -DNBDT-NW. The atomic displacements in alkyl chains are denoted by blue arrows.

equals  $0.60t_d$  when we do not consider the anharmonicity. This result suggests that anharmonicity cannot be ignored for quantitative assessment of the transfer integral fluctuation in  $C_{10}$ -DNBDT-NW. The total amount of the transfer integral fluctuation for  $t_c$  with anharmonicity (without anharmonicity) is  $0.062t_c$  ( $0.064t_c$ ). The reason why the  $\Delta t_c$  value does not depend on the presence of the anharmonicity of phonons is that the magnitudes of the e-ph coupling constants of  $t_c$  for  $I$ ,  $J$ ,  $L$ , and  $M$  are negligibly small.

#### E. Calculation of hole mobility based on transient localization theory

We estimate the hole mobility of each OSC at 293 K based on the transient localization theory. We use the open-source code in Refs. [11,66]. The values of  $t_{MN}$  and  $\Delta t_{MN}$  are set to the above-mentioned values in Secs. III C–III E. Typical phonon energy  $\hbar/\tau$  defined in Ref. [11] is set to 5 meV for tetracene and rubrene, which is the same as the value used in Ref. [11], and 1 meV for  $C_{10}$ -DNBDT-NW, which corresponds to the frequency of mode  $I$ . The size of a supercell and the number of samplings are  $40 \times 40 \times 1$  and 50, respectively. We check the convergence of the size of a supercell in each OSC. The obtained hole mobilities are  $\mu_b = 6.6 \pm 0.3 \text{ cm}^2/\text{Vs}$  in tetracene,  $\mu_b = 78 \pm 3 \text{ cm}^2/\text{Vs}$  in rubrene, and  $\mu_c = 46 \pm 3 \text{ cm}^2/\text{Vs}$  in  $C_{10}$ -DNBDT-NW. While the relative relation of the magnitudes of calculated hole mobilities is consistent with that evaluated from the experimental transfer characteristics in FETs, the calculated hole-mobility values themselves are two to three times as large as the corresponding experimental values [3,4,29]. These overestimations may originate from the  $\Gamma$ -point approximation since it un-

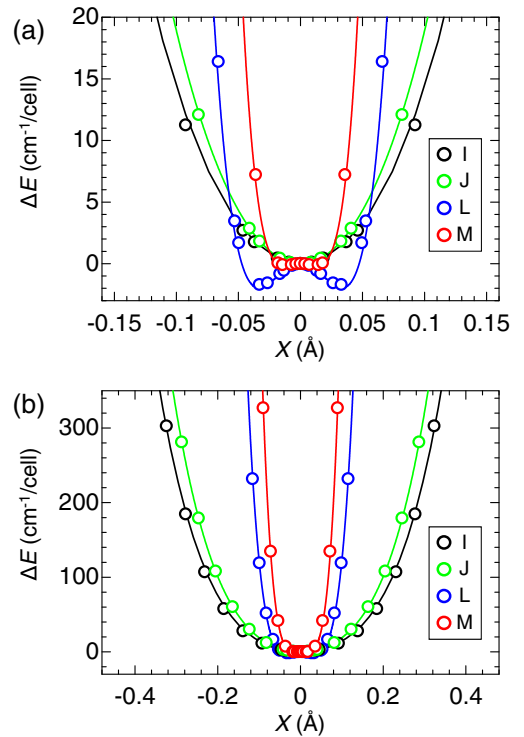


FIG. 14. Potential curves of low-frequency modes  $I$  and  $J$ , and imaginary frequency modes  $L$  and  $M$  in  $C_{10}$ -DNBDT-NW. Solid lines are fitting curves with a quartic function, (a)  $\Delta E < 20 \text{ cm}^{-1}/\text{cell}$ , (b)  $\Delta E < 350 \text{ cm}^{-1}/\text{cell}$ . The definition of  $X$  is the same as in Fig. 2.

derestimates the fluctuations of the transfer integrals. There are several papers reporting that experimental mobilities of OSCs were reproduced using the transient localization theory combined with first principle calculations [10,23,24,67,68], some of which computed the mobility of rubrene [10,23,24]. We expect that the extension of our methodology to the supercell should provide more accurate charge mobilities, while it requires high computational costs.

#### G. Comparison of three OSCs

Finally, we compare tetracene, rubrene, and  $C_{10}$ -DNBDT-NW from the viewpoint of transfer integrals and phonons. The carrier mobility averaged over the herringbone plane  $\mu_{\text{ave}}$  in the equilibrium structure depends on not only absolute values of the transfer integrals but also the sign of their products. One of the preferred conditions of OSCs showing high  $\mu_{\text{ave}}$  is that the absolute values of the transfer integrals between the nearest neighbor sites are preferred to be close to each other and their product to have a positive sign [10]. Tetracene does not satisfy the condition about sign of transfer integrals ( $t_{a1}t_{d1}t_{d2} < 0$ ), while rubrene and  $C_{10}$ -DNBDT-NW satisfy it ( $t_b t_d^2 > 0$  for rubrene,  $t_c t_d^2 > 0$  for  $C_{10}$ -DNBDT-NW). When comparing  $C_{10}$ -DNBDT-NW and rubrene, both the transfer integrals along the crystal axis and along the diagonal axis are fairly large in  $C_{10}$ -DNBDT-NW, while the transfer integral along the diagonal axis is very small in rubrene as listed in Table II. Therefore,  $C_{10}$ -DNBDT-NW is the most promising material for having high  $\mu_{\text{ave}}$  in

TABLE VI. Anharmonicity of low-frequency modes and imaginary frequency modes in C<sub>10</sub>-DNBDT-NW at room temperature.

Mode	$\omega^{(3)}$ (cm <sup>-1</sup> )	$\alpha_\lambda$	$\beta_\lambda$	$\sigma_{c,\text{harm}}^2$ (meV <sup>2</sup> )	$\sigma_{c,\text{anharm}}^2$ (meV <sup>2</sup> )	$\sigma_{d,\text{harm}}^2$ (meV <sup>2</sup> )	$\sigma_{d,\text{anharm}}^2$ (meV <sup>2</sup> )
<i>I</i>	7.7	0	0.018	0	0	470	170
<i>J</i>	8.8	0	0.014	3.3	1.3	110	40
<i>L</i>	12.8i	0	0.42		0.0057		0.053
<i>M</i>	9.0i	0	4.0		0		4.6

these OSCs from the viewpoint of transfer integrals in the equilibrium structure.

As mentioned in Sec. IV D, mode *D* in tetracene and mode *I* in C<sub>10</sub>-DNBDT-NW play important roles on the fluctuations of transfer integrals, both of which are the translational modes along the out-of-plane directions. On the other hand, in rubrene, the e-ph coupling constants of this mode (*A<sub>u</sub>* mode, 19.4 cm<sup>-1</sup>) become zero due to the symmetry. This suggests that the high crystal symmetry increases the carrier mobility in rubrene.

The strong modulations of transfer integrals by thermally induced out-of-plane molecular translations observed in tetracene and C<sub>10</sub>-DNBDT-NW originate not only from the large e-ph couplings but also from the low-frequency values. The translational mode along the out-of-plane direction has the lowest frequency among the optical phonon modes in the three OSCs in common, and thus this mode can be thermally excited with large amplitudes. The harmonic frequencies of the out-of-plane translational modes,  $\omega_{\text{OPT}}$ , in tetracene, rubrene, and C<sub>10</sub>-DNBDT-NW are 32.1, 19.4, and 7.7 cm<sup>-1</sup>, respectively. We consider the reason for small  $\omega_{\text{OPT}}$  in C<sub>10</sub>-DNBDT-NW as follows. The frequency  $\omega_{\text{OPT}}$  is proportional to  $\sqrt{k_{\text{OPT}}/M_{\text{mole}}}$ , where  $k_{\text{OPT}}$  is the intermolecular force constant corresponding to the out-of-plane translation and the  $M_{\text{mole}}$  is the molecular mass. The ratio of  $1/\sqrt{M_{\text{mole}}}$  in the three OSCs is tetracene: rubrene: C<sub>10</sub>-DNBDT-NW = 1: 0.655: 0.560, while the ratio of  $\omega_{\text{OPT}}$  is 1: 0.60: 0.24. Therefore, the small  $\omega_{\text{OPT}}$  in C<sub>10</sub>-DNBDT-NW cannot be explained solely by the large  $M_{\text{mole}}$ .  $k_{\text{OPT}}$  is considered to be proportional to  $M_{\text{mole}}\omega_{\text{OPT}}^2$ .  $M_{\text{mole}}\omega_{\text{OPT}}^2 = 1.4, 1.2,$  and  $0.25$  nN/Å for tetracene, rubrene, and C<sub>10</sub>-DNBDT-NW.  $k_{\text{OPT}}$  in tetracene and rubrene are not very different, while that in C<sub>10</sub>-DNBDT-NW is about five times smaller than the others. This result suggests that the causes for small harmonic frequency for the out-of-plane translational mode in C<sub>10</sub>-DNBDT-NW are both the large molecular mass and the small force constant.

## V. SUMMARY

In this paper, we examined the mode-resolved variances of transfer integrals originated from thermally excited intermolecular phonons in tetracene, rubrene, and C<sub>10</sub>-DNBDT-NW based on DFT. The calculated IR/Raman spectra nicely reproduced the experimental results, which demonstrates the validity of the vibrational calculations presented here. The introductions of the frequency correction and the possible anharmonicity enable us to calculate the accurate evaluation of the transfer integral fluctuation in C<sub>10</sub>-DNBDT-NW. We identified the intermolecular vibrational modes which strongly modulate the transfer

integral. The comparison of three OSCs in terms of the transfer integrals and out-of-plane intermolecular vibration was reported. Although the methodology introduced in this paper needs relatively high computational cost, it can give the highly accurate frequencies and nonlocal e-ph coupling constants of  $\Gamma$ -point phonons.

CCDC 1995124 contains the supplemental crystallographic data for C-DNBDT at 296 K. These data can be obtained free of charge from The Cambridge Crystallographic Data Centre [28].

## ACKNOWLEDGMENTS

This work was supported in part by the Japan Society for the Promotion of Science (JSPS) (Projects No. JP18K13476 and No. JP18H01166) and by CREST (Grant No. JPMJCR1661), Japan Science and Technology Agency. T. Otaki was supported by JSPS through the Program for Leading Graduate Schools (MERIT). T. Okamoto was supported by the JST-PRESTO program ‘‘Scientific Innovation for Energy Harvesting Technology’’ (Grant No. JPMJPR17R2).

## APPENDIX

In this Appendix, we show that the corrected frequency  $\omega_\lambda^{(2)}$  is more accurate than  $\omega_\lambda^{(1)}$ . We define the difference between  $W$  and  $W^{(\text{num})}$  as  $\Delta W^{(\text{err})}$ :

$$W = W^{(\text{num})} + \Delta W^{(\text{err})}. \quad (\text{A1})$$

The corrected eigenvalue of  $W$  is derived by using the first order perturbation theory in which  $\Delta W^{(\text{err})}$  is treated as a perturbative term:

$$\begin{aligned} \omega_\lambda^2 &= \{\omega_\lambda^{(1)}\}^2 + \{e_\lambda^{(\text{num})}\}^T \Delta W^{(\text{err})} \{e_\lambda^{(\text{num})}\} + O(\{\Delta W^{(\text{err})}\}^2) \\ &= \{e_\lambda^{(\text{num})}\}^T W \{e_\lambda^{(\text{num})}\} + O(\{\Delta W^{(\text{err})}\}^2). \end{aligned} \quad (\text{A2})$$

$\sqrt{\{e_\lambda^{(\text{num})}\}^T W \{e_\lambda^{(\text{num})}\}}$  is the corrected frequency whose error is  $O(\{\Delta W^{(\text{err})}\}^2)$ , whereas the error of  $\omega_\lambda^{(1)}$  is  $O(\Delta W^{(\text{num})})$ . The relation between  $\{e_\lambda^{(\text{num})}\}^T W \{e_\lambda^{(\text{num})}\}$  and  $\Delta E_\lambda(Q_\lambda)$  is derived as

$$\begin{aligned} \Delta E_\lambda(Q_\lambda) &\equiv V(\mathbf{u}_\lambda^{(\text{num})}) - V(0) \\ &= \frac{1}{2} \frac{\partial^2 V}{\partial u_{i\alpha} \partial u_{j\beta}} u_{\lambda,i\alpha}^{(\text{num})} u_{\lambda,j\beta}^{(\text{num})} + O(Q_\lambda^3) \\ &= \frac{1}{2} \{e_\lambda^{(\text{num})}\}^T W \{e_\lambda^{(\text{num})}\} Q_\lambda^2 + O(Q_\lambda^3). \end{aligned} \quad (\text{A3})$$

Then,  $\omega_\lambda^{(2)} = \sqrt{\{e_\lambda^{(\text{num})}\}^T W \{e_\lambda^{(\text{num})}\}}$  is immediately obtained from this equation, and thus  $\omega_\lambda^{(2)}$  is found to be a corrected frequency which is more accurate than  $\omega_\lambda^{(1)}$ .

- [1] C. Reese, M. Roberts, M. M. Ling, and Z. Bao, *Mater. Today* **7**, 20 (2004).
- [2] M. E. Gershenson, V. Podzorov, and A. F. Morpurgo, *Rev. Mod. Phys.* **78**, 973 (2006).
- [3] J. Takeya, M. Yamagishi, Y. Tominari, R. Hirahara, and Y. Nakazawa, *Appl. Phys. Lett.* **90**, 102120 (2007).
- [4] C. Mitsui, T. Okamoto, M. Yamagishi, J. Tsurumi, K. Yoshimoto, K. Nakahara, J. Soeda, Y. Hirose, H. Sato, A. Yamano, T. Uemura, and J. Takeya, *Adv. Mater.* **26**, 4546 (2014).
- [5] V. Podzorov, E. Menard, J. A. Rogers, and M. E. Gershenson, *Phys. Rev. Lett.* **95**, 226601 (2005).
- [6] J. Tsurumi, H. Matsui, T. Kubo, R. Häusermann, C. Mitsui, T. Okamoto, S. Watanabe, and J. Takeya, *Nat. Phys.* **13**, 994 (2017).
- [7] V. Podzorov, E. Menard, A. Borissov, V. Kiryukhin, J. A. Rogers, and M. E. Gershenson, *Phys. Rev. Lett.* **93**, 086602 (2004).
- [8] S. Fratini, D. Mayou, and S. Ciuchi, *Adv. Funct. Mater.* **26**, 2292 (2016).
- [9] S. Ciuchi, S. Fratini, and D. Mayou, *Phys. Rev. B* **83**, 081202(R) (2011).
- [10] S. Fratini, S. Ciuchi, D. Mayou, G. Trambly de Laissardière, and A. Troisi, *Nat. Mater.* **16**, 998 (2017).
- [11] T. Nematlaram, S. Ciuchi, X. Xie, S. Fratini, and A. Troisi, *J. Phys. Chem. C* **123**, 6989 (2019).
- [12] T. Okamoto, *Polym. J.* **51**, 825 (2019).
- [13] P. Ordejón, D. Boskovic, M. Panhans, and F. Ortman, *Phys. Rev. B* **96**, 035202 (2017).
- [14] N. Marzari, A. A. Mostofi, J. R. Yates, I. Souza, and D. Vanderbilt, *Rev. Mod. Phys.* **84**, 1419 (2012).
- [15] C. Motta and S. Sanvito, *J. Chem. Theory Comput.* **10**, 4624 (2014).
- [16] H. Ishii, N. Kobayashi, and K. Hirose, *Phys. Rev. B* **95**, 035433 (2017).
- [17] X. Xie, A. S. Bonilla, and A. Troisi, *J. Chem. Theory Comput.* **14**, 3752 (2018).
- [18] R. S. S. Carrera, P. Paramonov, G. M. Day, V. Coropceanu, and J. L. Brédas, *J. Am. Chem. Soc.* **132**, 14437 (2010).
- [19] T. Fukami, H. Ishii, N. Kobayashi, T. Uemura, K. Sakai, Y. Okada, J. Takeya, and K. Hirose, *Appl. Phys. Lett.* **106**, 143302 (2015).
- [20] A. Girlando, L. Grisanti, M. Masino, I. Bilotti, A. Brillante, R. G. D. Valle, and E. Venuti, *Phys. Rev. B* **82**, 035208 (2010).
- [21] G. Schweicher, G. D'Avino, M. T. Ruggiero, D. J. Harkin, K. Broch, D. Venkateshvaran, G. Liu, A. Richard, C. Ruzié, J. Armstrong, A. R. Kennedy, K. Shankland, K. Takimiya, Y. H. Geerts, J. A. Zeitler, S. Fratini, and H. Sirringhaus, *Adv. Mater.* **31**, 1902407 (2019).
- [22] M. T. Ruggiero, S. Ciuchi, S. Fratini, and G. D'Avino, *J. Phys. Chem. C* **123**, 15897 (2019).
- [23] S. Giannini, A. Carof, M. Ellis, H. Yang, O. G. Ziogos, S. Ghosh, and J. Blumberger, *Nat. Commun.* **10**, 3843 (2019).
- [24] T. Nematlaram, D. Padula, A. Landi, and A. Troisi, *Adv. Funct. Mater.* **30**, 2001906 (2020).
- [25] H. Ishii, J. Inoue, N. Kobayashi, and K. Hirose, *Phys. Rev. B* **98**, 235422 (2018).
- [26] D. Holmes, S. Kumaraswamy, A. J. Matzger, and K. P. C. Vollhardt, *Chem. Eur. J.* **5**, 3399 (1999).
- [27] O. D. Jurchescu, A. Meetsma, and T. T. M. Palstra, *Acta Crystallogr., Sect. B* **62**, 330 (2006).
- [28] [www.ccdc.cam.ac.uk/data\\_request/cif](http://www.ccdc.cam.ac.uk/data_request/cif)
- [29] C. Reese, W. J. Chung, M. M. Ling, M. Roberts, and Z. Bao, *Appl. Phys. Lett.* **89**, 202108 (2006).
- [30] C. Reese and Z. Bao, *Adv. Mater.* **19**, 4535 (2007).
- [31] E. G. Bittle, A. J. Biacchi, L. A. Fredin, A. A. Herzing, T. C. Allison, A. R. H. Walker, and D. J. Gundlach, *Commun. Phys.* **2**, 29 (2019).
- [32] Previous research shows  $t_b \approx t_d \approx 50$  meV [4].
- [33] R. Dovesi, V. R. Saunders, C. Roetti, R. Orlando, C. M. Zicovich-Wilson, F. Pascale, B. Civalieri, K. Doll, N. M. Harrison, I. J. Bush, P. D'Arco, M. Llunell, M. Causà, Y. Noël, L. Maschio, A. Erba, M. Rérat, and S. Casassa, *CRYSTAL17 User's Manual* (University of Torino, Torino, 2017).
- [34] A. D. Becke, *J. Chem. Phys.* **98**, 5648 (1993).
- [35] P. J. Stephens, F. J. Devlin, C. F. Chabalowski, and M. J. Frisch, *J. Phys. Chem.* **98**, 11623 (1994).
- [36] P. C. Hariharan and J. A. Pople, *Theor. Chim. Acta* **28**, 213 (1973).
- [37] S. Grimme, J. Antony, S. Ehrlich, and H. Krieg, *J. Chem. Phys.* **132**, 154104 (2010).
- [38] H. J. Monkhorst and J. D. Pack, *Phys. Rev. B* **13**, 5188 (1976).
- [39] D. V. Oliveira, J. Laun, M. F. Peintinger, and T. Bredow, *J. Comput. Chem.* **40**, 2364 (2019).
- [40] F. Pascale, C. M. Zicovich-Wilson, F. López Gejo, B. Civalieri, R. Orlando, and R. Dovesi, *J. Comput. Chem.* **25**, 888 (2004).
- [41] C. M. Zicovich-Wilson, F. Pascale, C. Roetti, V.R. Saunders, R. Orlando, and R. Dovesi, *J. Comput. Chem.* **25**, 1873 (2004).
- [42] K. K. Irikura, R. D. Johnson III, and R. N. Kacker, *J. Phys. Chem. A* **109**, 8430 (2005).
- [43] S. Dall'Olio, R. Dovesi, and R. Resta, *Phys. Rev. B* **56**, 10105 (1997).
- [44] R. Dovesi, B. Kirtman, L. Maschio, J. Maul, F. Pascale, and M. Rérat, *J. Phys. Chem. C* **123**, 8336 (2019).
- [45] M. Cardona and G. Güntherodt, *Light Scattering in Solids II* (Springer Verlag, Berlin, 1982).
- [46] M. Veithen, X. Gonze, and Ph. Ghosez, *Phys. Rev. B* **71**, 125107 (2005).
- [47] W. Hayes and R. Loudon, *Scattering of Light by Crystals* (Wiley, New York, 1978).
- [48] S. A. Prosandeev, U. Waghmare, I. Levin, and J. Maslar, *Phys. Rev. B* **71**, 214307 (2005).
- [49] L. Maschio, B. Kirtman, M. Rérat, R. Orlando, and R. Dovesi, *J. Chem. Phys.* **139**, 164101 (2013).
- [50] L. Maschio, B. Kirtman, M. Rérat, R. Orlando, and R. Dovesi, *J. Chem. Phys.* **139**, 164102 (2013).
- [51] E. F. Valeev, V. Coropceanu, D. A. da Silva Filho, S. Salman, and J. L. Brédas, *J. Am. Chem. Soc.* **128**, 9882 (2006).
- [52] B. Baumeier, J. Kirkpatrick, and D. Andrienko, *Phys. Chem. Chem. Phys.* **12**, 11103 (2010).
- [53] Y. Kuroda, H. Ishii, S. Yoshino, and N. Kobayashi, *Jpn. J. Appl. Phys.* **58**, SIIB27 (2019).
- [54] J. Yamauchi, M. Tsukada, S. Watanabe, and O. Sugino, *Phys. Rev. B* **54**, 5586 (1996).
- [55] O. Sugino and A. Oshiyama, *Phys. Rev. Lett.* **68**, 1858 (1992).
- [56] For information about the xTAPP code and the norm-conserving pseudopotentials for PBE functional, see <http://xtapp.cp.is.s.u-tokyo.ac.jp/>



- [57] J. P. Perdew, K. Burke, and M. Ernzerhof, *Phys. Rev. Lett.* **77**, 3865 (1996).
- [58] J. P. Perdew, K. Burke, and M. Ernzerhof, *Phys. Rev. Lett.* **78**, 1396 (1997).
- [59] F. Ortmann, F. Bechstedt, and K. Hannewald, *Phys. Status Solidi B* **248**, 511 (2011).
- [60] T. Tadano and S. Tsuneyuki, *Phys. Rev. B* **92**, 054301 (2015).
- [61] E. Venuti, R. G. D. Valle, L. Farina, A. Brillante, M. Masino, and A. Girlando, *Phys. Rev. B* **70**, 104106 (2004).
- [62] E. Venuti, I. Bilotti, R. G. D. Valle, A. Brillante, P. Ranzieri, M. Masino, and A. Girlando, *J. Phys. Chem. C* **112**, 17416 (2008).
- [63] H. Yada, R. Uchida, H. Sekine, T. Terashige, S. Tao, Y. Matsui, N. Kida, S. Fratini, S. Ciuchi, Y. Okada, T. Uemura, J. Takeya, and H. Okamoto, *Appl. Phys. Lett.* **105**, 143302 (2014).
- [64] V. Coropceanu, J. Cornil, D. A. da Silva Filho, Y. Olivier, R. Silbey, and J. L. Brédas, *Chem. Rev.* **107**, 926 (2007).
- [65] C. Sutton, J. S. Sears, V. Coropceanu, and J. L. Brédas, *J. Phys. Chem. Lett.* **4**, 919 (2013).
- [66] We use the open source code to compute hole mobilities released by Sergio Ciuchi (<https://github.com/CiuK1469/TransLoc>).
- [67] T. F. Harrelson, V. Dantanarayana, X. Xie, C. Koshnick, D. Nai, R. Fair, S. A. Nuñez, A. K. Thomas, T. L. Murrey, M. A. Hickner, J. K. Grey, J. E. Anthony, E. D. Gomez, A. Troisi, R. Faller, and A. J. Moulé, *Mater. Horiz.* **6**, 182 (2019).
- [68] V. Dantanarayana, T. Nematiram, D. Vong, J. E. Anthony, A. Troisi, K. N. Cong, N. Goldman, R. Faller, and A. J. Moulé, *J. Chem. Theory Comput.* **16**, 3494 (2020).